THRUST AREA REPORT • UCRL-ID-125470

Computational Electronics and Electromagnetics

Clifford C. Shang,
Thrust Area Leader

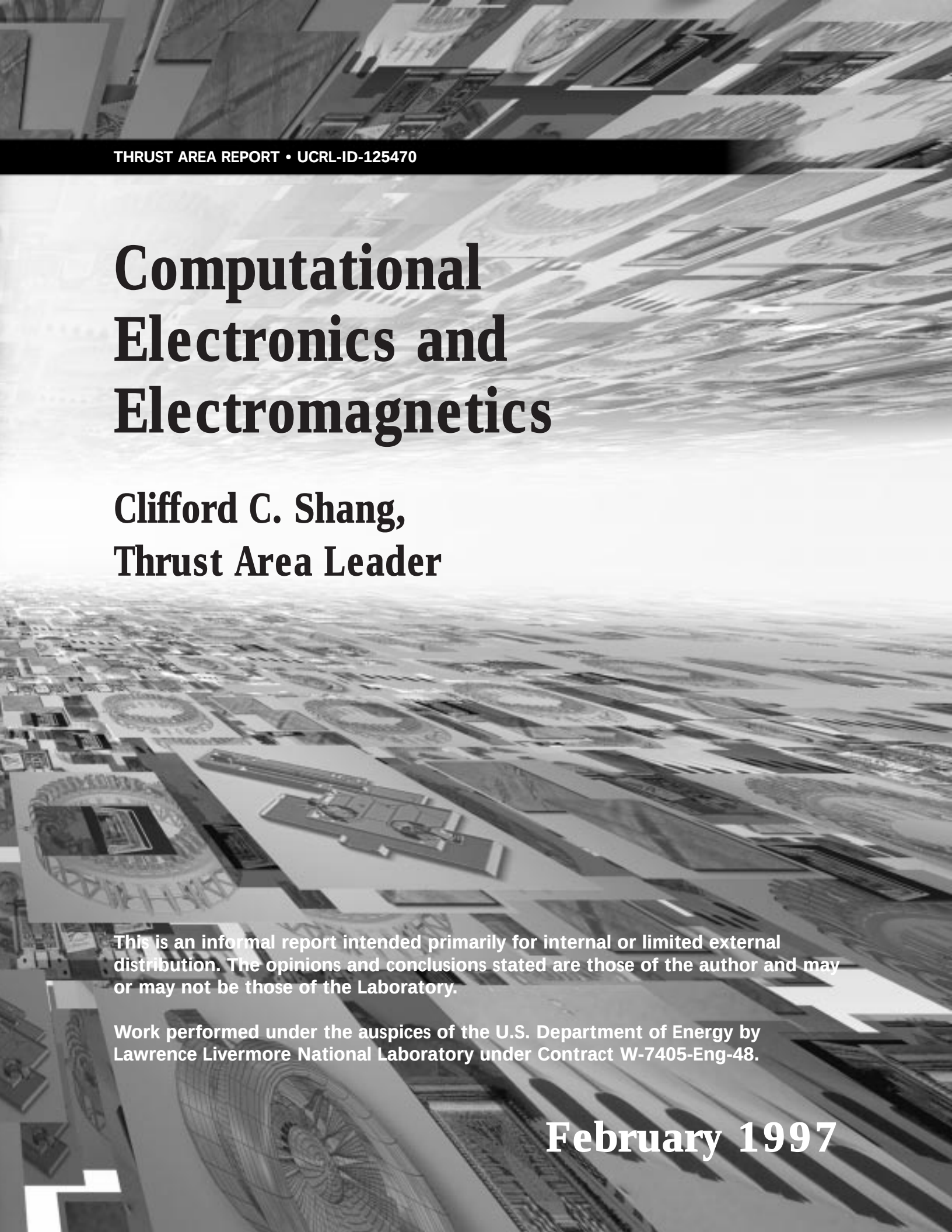

Work performed under the auspices of the U.S. Department of Energy by Lawrence Livermore National Laboratory under Contract W-7405-Eng-48.

February 1997

THRUST AREA REPORT • UCRL-ID-125470

Computational Electronics and Electromagnetics

Clifford C. Shang,
Thrust Area Leader

Reprinted from Engineering Research, Development and Technology
FY 96 UCRL 53868-96

February 1997

Clifford C. Shang, Thrust Area Leader

The Computational Electronics and Electromagnetics thrust area at Lawrence Livermore National Laboratory serves as the focal point for engineering R&D activities for developing computer-based design, analysis, and tools for theory.

Key representative applications include design of particle accelerator cells and beamline components; engineering analysis and design of high-power components, photonics and optoelectronics circuit design; EMI susceptibility analysis; and antenna synthesis.

The FY-96 technology-base effort focused code development on (1) accelerator design codes; (2) 3-D massively parallel, object-oriented time-domain EM codes; (3) material models; (4) coupling and application of engineering tools for analysis and design of high-power components; (5) 3-D spectral-domain CEM tools; and (6) enhancement of laser drilling codes.

Joint efforts with the Power Conversion Technologies thrust area include development of antenna systems for compact, high-performance radar, in addition to novel, compact Marx generators.

Computational Electronics and Electromagnetics

1

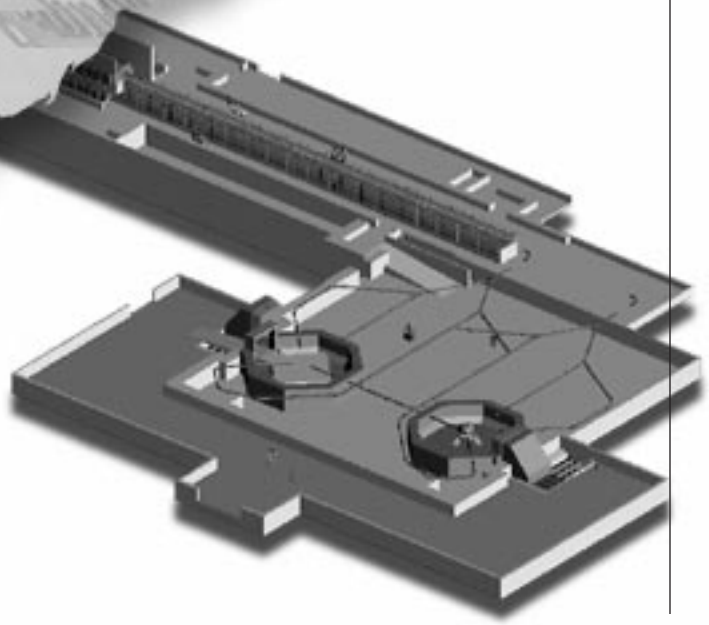

1. Computational Electronics and Electromagnetics

Three-Dimensional Electromagnetic Modeling of Wakefields in Accelerator Components

Brian R. Poole and Wang C. Ng
Defense Sciences Engineering Division
Electronics Engineering

George J. Caporaso
Inertial Confinement Fusion
Laser Programs

This report describes continuing work on the development of computational wakefield tools for the design of accelerator components for the advanced radiographic machine (ARM). New massively-parallel 3-D time-domain electromagnetic codes now under development using conforming unstructured meshes with advanced radiation boundary conditions allow a substantial increase in the geometric fidelity of the structures being modeled, as well as a more suitable truncation of the problem space. A variety of 3-D structures are tested with an existing cubical cell finite-difference time-domain (FDTD) code and the wake impedances are compared with simple analytic models for the structures. These results provide a set of benchmarks for testing the new time-domain codes and provide insight into the wakefield physics of the structures. Structures under consideration include a stripline beam position monitor and a circular aperture in a circular waveguide. We have achieved excellent agreement for the monopole and dipole impedances for the models below the cut-off frequency of the beamline for a stiff electron beam moving parallel to the beamline axis. We are extending the wakefield calculations to include beams that have more complex trajectories within the structure, which will allow more realistic physics to be included in calculations for ARM.

Introduction

In FY-95 and FY-96, we began development of tools to analyze the interaction of relativistic charged-particle beams with accelerator components. This work is primarily motivated by the need for advanced modeling techniques for problems relevant to the design of electron beam accelerators for ARM. The ARM requires multiple electron beams to be directed from various lines of sight onto a target for the generation of x rays for use in pulsed radiography applications. A cost-effective design requires that the electron beams be generated from a single linear induction accelerator.

To accomplish the generation of multiple electron beams, several beam kickers and beamline septums are used. A beam kicker is a structure designed to spatially separate an electron beam pulse into two separate electron beam pulses. The kicker structure and septum region are shown schematically in **Fig. 1**. The kicker, which consists of two pairs of transmission lines enclosed in a cylindrical beamline, is designed to steer the relativistic electron beam (REB) into the correct trajectory for transport into a magnetic field that bends the beam into the downstream beamlines.

One pair of transmission lines is grounded at each end by connecting them to the beam pipe. The other pair is connected to external transmission lines that can be driven by an external modulator at one end of the structure. The other ends of the driven transmission lines are connected to matched loads. By alternating the polarity of each applied electromagnetic pulse on the driven transmission lines, alternate electron beam pulses can be directed into each of the two downstream beam transport systems.

After the electron beam is separated into two beam pulses, each beam pulse is directed into the appropriate beamline by the applied magnetic field in the septum region. The magnetic field has opposite field directions on each side of the plane separating

the downstream beam transport systems to bend each beam into the appropriate system.

Understanding the wake properties of these structures is crucial to the design of accelerator components for the ARM. For high current electron beams, the ability to steer the beam through the kicker and septum regions is strongly dependent on the wake properties of these structures. If the kicker possesses a strong transverse dipole impedance, a high current electron beam can induce large voltages on the steering transmission lines.

Since these voltages may be comparable to the externally applied voltage, the ability to steer the beam may be impaired, and improved dynamic control of the external pulser voltage will be required to compensate for the beam induced steering. Similarly, the presence of a large aperture in the septum region may lead to deleterious effects on beam quality.

As discussed in a previous report,[1] it is not practical with our current cubical cell FDTD codes to model the full scale kicker and septum regions, due to the large mesh sizes required for the model and the long run times required for low frequency resolution. Also, because of the lack of advanced radiation boundary conditions, boundary conditions cannot be applied to the oblique surfaces associated with the exit beamlines of the septum region. However, confidence in analysis techniques can be achieved by modeling smaller scale devices similar in design to these structures, such as the stripline beam position monitor and the waveguide aperture.

Wakefield Analysis

A crucial area in the design of linear induction accelerators and beam transport systems is the understanding of the wakefields generated by a charge bunch as it is transported through the system. As this charge bunch passes a perturbation in an accelerator structure, an electromagnetic wakefield is generated which can re-interact with the charged particle beam. This process can lead to degradation of the beam, or worse, can lead to beam breakup instabilities with the resultant loss of beam quality at the target.

Consider a beam transport system consisting of a cylindrical drift tube with some perturbation in its structure followed again by a cylindrical drift tube, as shown in **Fig. 2**. The perturbation is not necessarily cylindrically symmetric and may consist of features such as changes in the cross-section, apertures in the wall, or different material properties. An axial current of the form defined in **Eq. 1** is used to represent the current due to a moving source charge Q in the beam pipe.

$$J_z = I_0 \delta\left(r - r_0\right)\delta\left(\phi - \phi_0\right)\delta\left(vt - z\right) \qquad (1)$$

Here r_0 and ϕ_0 represent the transverse location of the source charge in the accelerating structure, z is the axial location of the source at time t, I_0 is the strength of the current source, and $\delta(vt - z)$ represents the location of the source charge, Q. If we were modeling a charge bunch, the delta function $\delta(vt - z)$ would be replaced by a function $f(vt - z)$ representing the shape of the charge bunch. Typically a narrow Gaussian pulse is used as the source function in our modeling to approximate a delta function while preserving a "clean" turn on of the sources.

In this analysis we are interested in the response of a test charge that is trailing the source charge by a distance $s = vt - z$. The electromagnetic fields in the structure are considered to be the sum of multipole modes as shown in **Eq. 2:**

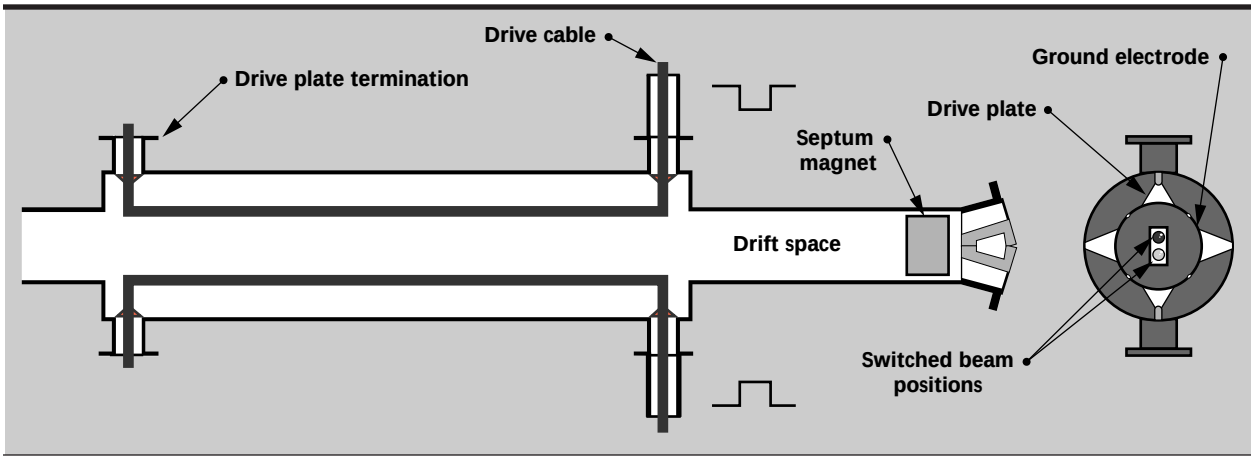

Figure 1. Schematic representation of the kicker. The kicker spatially separates the electron beam and the septum magnet bends the individual beams into the appropriate beamline.

$$\psi(r,z,t) = \sum_{m=0}^{\infty} \left[\psi_m^p(r,z,t)\cos(m\phi) + \psi_m^q(r,z,t)\sin(m\phi) \right] \quad (2)$$

where ψ represents any electromagnetic field component, and ψ_m^p and ψ_m^q represent the various multipole coefficients for the specific field component. Since the force on a test charge q due to the electromagnetic field generated by the source point charge Q is given by

$$\mathbf{F} = q(\mathbf{E} + \mathbf{v} \times \mathbf{B}) \quad (3)$$

it is convenient to define the concept of an impulse wake potential as

$$\mathbf{W}(s) = \int_{-\infty}^{\infty} (\mathbf{E} + \mathbf{v} \times \mathbf{B})\Big|_{t=(s+z)/v} dz. \quad (4)$$

The impulse wake potential for each multipole mode can be determined by applying **Eq. 4** to each field component as defined in **Eq. 2**. A wake impedance function can be defined by taking the Fourier transform over the variable $s = vt - z$ of the wake potential for the longitudinal and transverse components of the force for each multipole mode. Since the strength of the multipole component of the source current is proportional to r_0^m, this factor is included in the definition of the vector wake impedance as

$$\mathbf{Z}_m(\omega) = \frac{1}{r_0^m I_0} \int_{-\infty}^{\infty} \mathbf{W}_m(s) e^{-i\omega s/v} ds \quad (5)$$

and represents a figure of merit defining the strength of the interaction of a charged-particle beam with an electromagnetic structure in both the longitudinal and transverse directions. It is desirable to keep the wake impedance function as small as possible to prevent undesirable coupling between the beam and the structure.

Progress

Modeling

TSAR is the primary 3-D electromagnetic field code used for analysis of these structures. TSAR uses a 3-D grid composed of cubical cells for the FDTD analysis, with each cell being assigned a given material property. The cell size is typically chosen to resolve the shortest wavelength expected in the problem and, in addition, must be chosen small enough to accurately model the smallest dimension in the model. To satisfy stability requirements for the FDTD field solver, the Courant stability condition for the time step must be satisfied. This condition is defined in **Eq. 6**

$$dt < \frac{1}{2c} dx \quad (6)$$

where dx is the length of the cell edge.

Beam Position Monitor

The stripline beam position monitor is discussed in some detail by Ng.[2] The beam position monitor consists of two pairs of strip transmission lines,

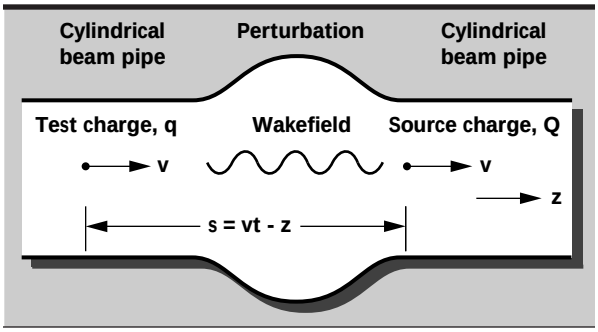

Figure 2. Geometry of a wakefield calculation. The source of the electromagnetic wakefield is the charge, Q. The spectral characteristics of the longitudinal and transverse forces are determined on a test charge, q subjected to the wakefield.

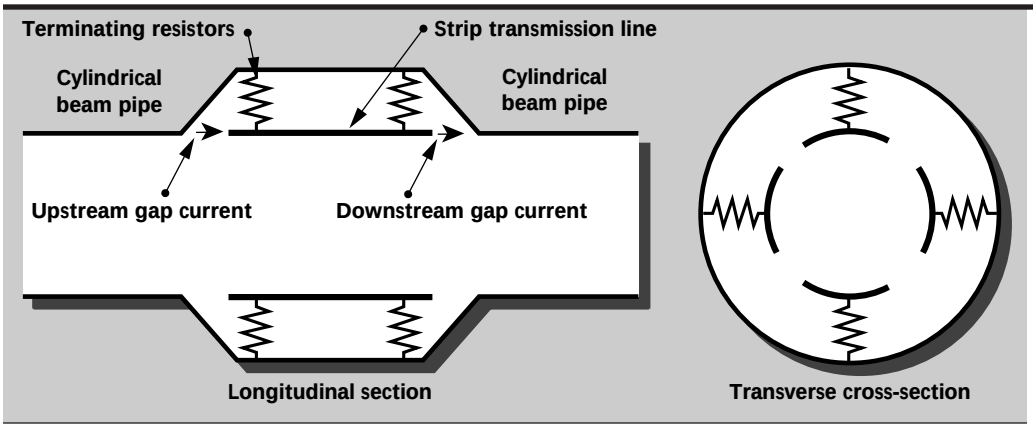

Figure 3. Schematic representation of the stripline beam position monitor.

shown schematically in **Fig. 3**. The 25-Ω terminating resistors were chosen based on a frequency domain calculation of the TEM impedance of the structure. For modeling purposes, the terminating resistors represent external coaxial transmission line feeds to the striplines. Even to represent the gross geometric characteristics of the structure using cubical cells requires a cell size of 0.5 mm, making the computational size of this problem 8×10^6 cells and requires a time step of .83 ps, as dictated by the Courant stability condition.

To accurately represent the details of the coaxial feeds would have required a much smaller cell size to have adequate geometric fidelity in the feed region. Therefore, it was decided to use simple wire resistors to model this region to minimize the computer memory requirements. The length of the striplines was 10 cm, which indicates a quarter-wavelength resonance of 750 MHz, allowing us to sufficiently resolve the low frequency behavior using 16000 time steps. Approximately 25 cm of beam transport line was used on each side of the beam position monitor to allow evanescent waves to decay and to minimize the effects of the MUR radiation boundary conditions applied to the axial boundaries of the problem space.

The structure is excited with a current distribution of the form defined in **Eq. 1**. Analytic expressions for the longitudinal monopole (m = 0) and transverse dipole (m = 1) impedances for a matched transmission line model of the beam position monitor are[2]

$$Z_{\parallel} = Z_s\left(\frac{\phi_s}{2\pi}\right)^2 \times\left[\sin^2\left(\frac{\omega L}{c}\right) + j\sin\left(\frac{\omega L}{c}\right)\cos\left(\frac{\omega L}{c}\right)\right] \quad (7)$$

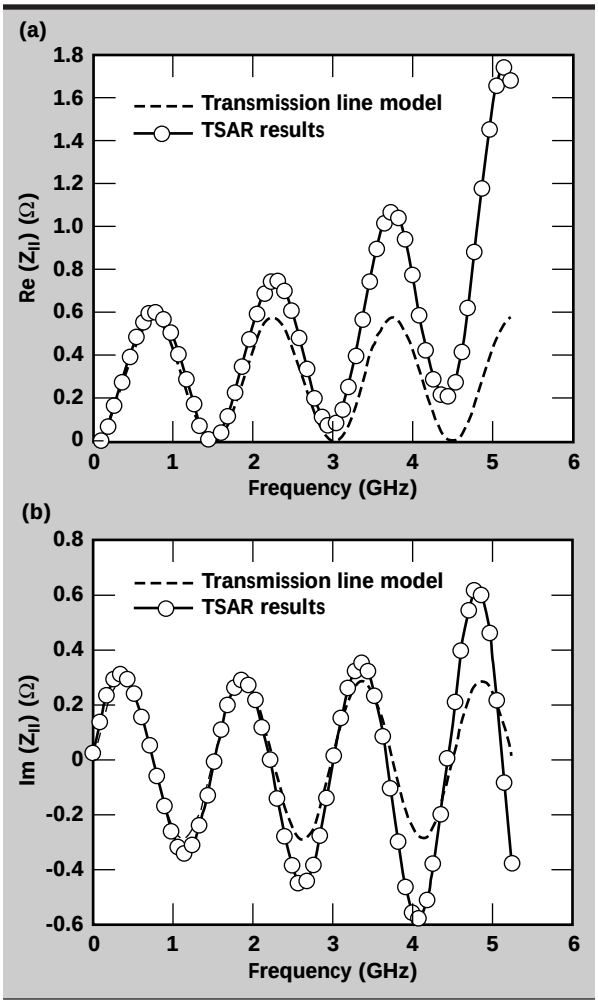

Figure 4. Code results and analytic results for the real (a) and imaginary (b) components of the longitudinal impedance of the stripline beam position monitor.

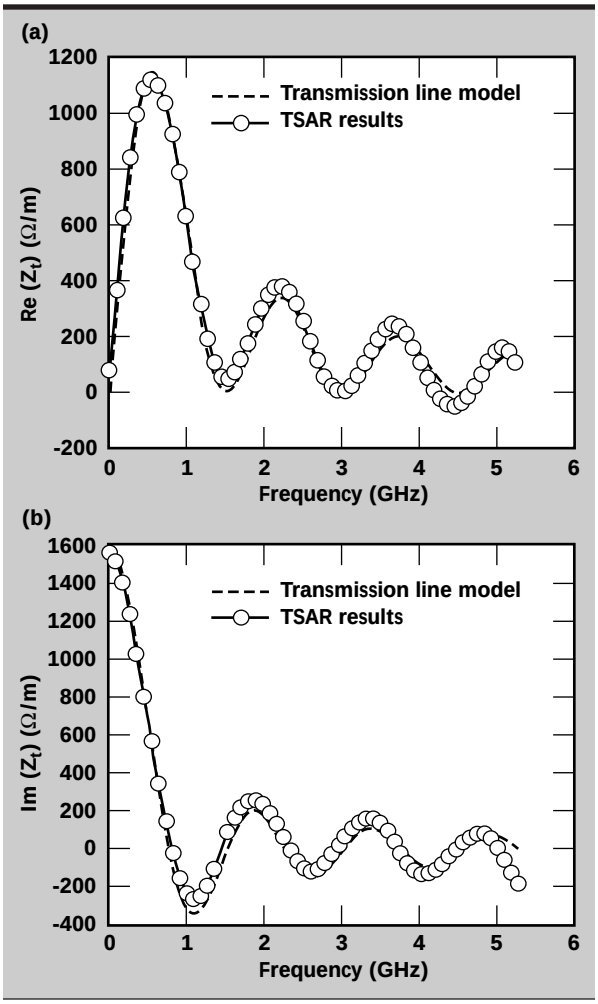

Figure 5. Code results and analytic results for the real (a) and imaginary (b) components of the transverse dipole impedance of the stripline beam position monitor.

$$Z_{\perp} = \frac{8cZ_s}{\pi^2 R_s^2}\left(\frac{1}{\omega}\right)\sin^2\left(\frac{\phi_s}{2}\right) \times\left[\sin^2\left(\frac{\omega L}{c}\right) + j\sin\left(\frac{\omega L}{c}\right)\cos\left(\frac{\omega L}{c}\right)\right]. \quad (8)$$

Figures 4 and **5** show comparisons of the analytic models with results obtained numerically through the TSAR modeling code for the longitudinal and transverse impedances, respectively. There is excellent low frequency agreement. The deviation at higher frequencies may be attributed to the high frequency impedance of the wire resistors which are not accurately represented by a cell size of 0.5 mm.

Circular Aperture in Circular Beamline

The impedance of coupling apertures in beam transport lines has been treated in the literature by Gluckstern[3] and Kurennoy.[4] In this section we consider a 3-cm diameter cylindrical beamline with either an 8-mm or a 3-cm circular waveguide connected at 90° to the beamline, as shown in **Fig. 6**. The 3 ports of the problem space are terminated with MUR radiation boundary conditions. A cell size of 0.5 mm is used to model both aperture problems. The length of the beamline is about 30 cm and the coupling waveguide is 3 cm long, resulting in a mesh of about 1.2×10^7 cells. An analytic expression for the low frequency transverse dipole impedance is given by **Eq. 9**.

$$Z_{\perp} = j\frac{2a^3 Z_0}{3\pi^2 R_0^4} f(w) \quad (9)$$

where Z_0 is the impedance of free space and $f(w)$ is a correction factor based on the length of the coupling guide and has a value of 0.562 for $w/a > 2$, as defined in Gluckstern.[3] In our model, $w = 3$ cm. For the 8-mm coupling guide **Eq. 9** gives an inductive transverse impedance of 18.1 Ω/m. The TSAR model predicts an inductive transverse impedance of 18.3 Ω/m for frequencies up to 6 GHz.

Figure 7 shows the TSAR results for the 3-cm large aperture case for the transverse impedance along with the low frequency asymptote for the reactive component of the impedance. The real part arises from the fact that the secondary coupling waveguide is only 3 cm long in the model and does not let low frequency fields evanesce sufficiently before reaching the MUR boundary condition on the coupling guide. This accounts for the resonance near the TE_{11} cutoff at 5.9 GHz.

Future Work

The calculations and modeling of wake impedances in this report are based on simple models of complex structures. The structures that need to be modeled are typically two orders of magnitude larger in volume, requiring more efficient volume meshing to effectively model the structures with a high degree of geometric fidelity. In addition, improvements to the radiation boundary conditions need to be implemented to model structures with more complicated truncations to the problem space, such as the oblique surfaces on the exit beamlines of the kicker septum region.

The new DSI-TIGER code under development includes such features as conforming grids, hybrid structured/unstructured grids, massively parallel capability, and new radiation boundary conditions. Conforming grids eliminate stair-casing errors associated with cubical cell codes and allow more realistic models to be developed for complicated structures. However, conforming unstructured non-orthogonal grids require typically 30 times the memory overhead compared to structured orthogonal grids. Hybrid grids can overcome this limitation by using conforming grids only near appropriate surfaces and structured grids elsewhere. New advanced radiation boundary conditions can also reduce the computational effort by allowing a closer truncation of the problem space.

New physics needs to be incorporated in existing and new codes to put prescribed electron beam trajectories in the accelerator problems. For example, in the kicker the electron beam does not follow a simple straight line trajectory parallel to the beamline axis. The interaction of the beam with the externally applied fields produces a trajectory in the structure as governed by the dynamical equations of motion in the externally prescribed electromagnetic field. Extensions to

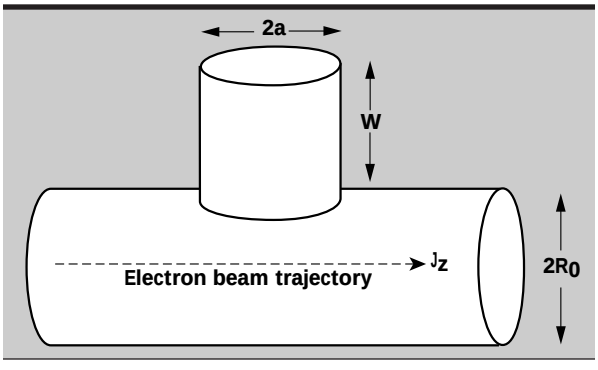

Figure 6. Schematic representation of the waveguide junction aperture problem.

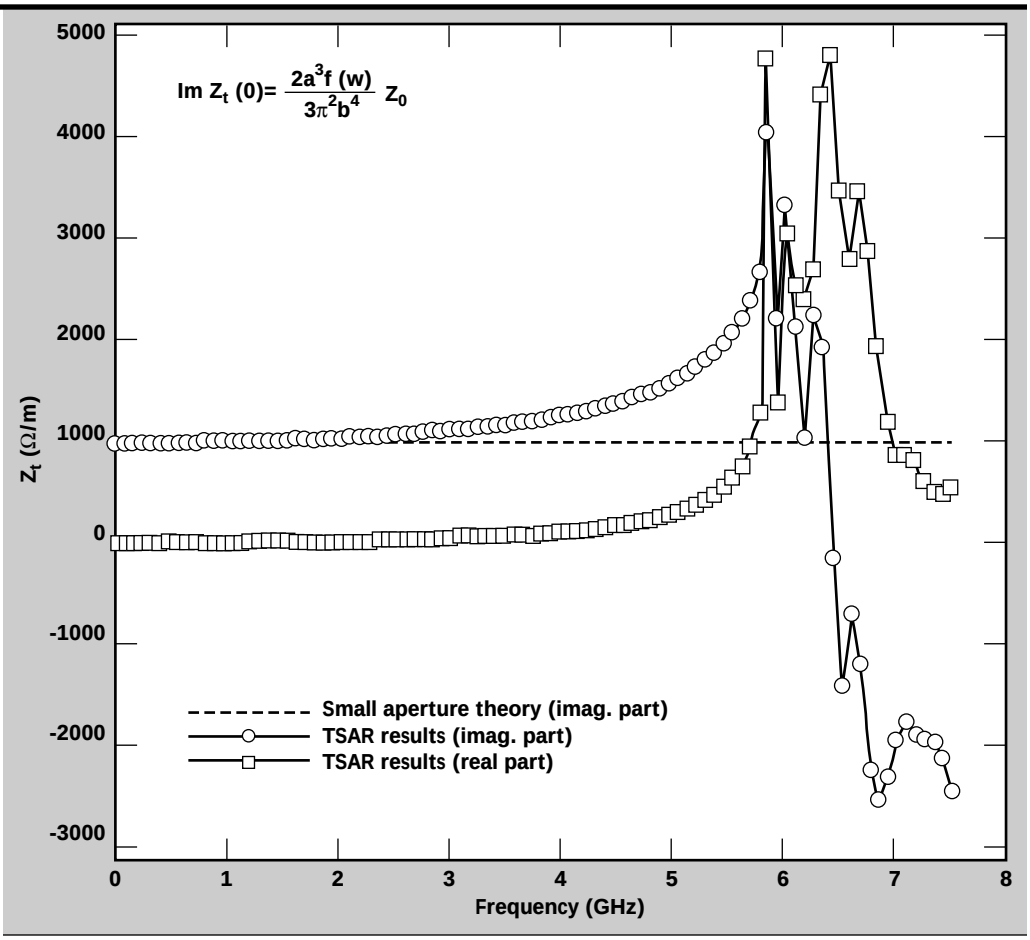

Figure 7. Transverse dipole impedance for the 3-cm large aperture waveguide junction. The resonance near 5.9 GHz is due to the TE_{11} cutoff. The real part of the impedance results from the fact that the short length of the coupling guide does not allow evanescent waves to sufficiently decay before reaching the MUR radiation boundary condition.

wakefield codes need to include the real prescribed electron beam trajectory to determine the wake properties of the structure.

Preliminary work in this area has already been applied to the TSAR cubical cell code with some success. However, proper interpretation of the results needs to be addressed to understand the wake physics in this regime. We are continuing work in this area by developing distributed impedance models of simple structures for complicated beam trajectories.

Acknowledgments

The authors wish to acknowledge discussions with S. Nelson of Lawrence Livermore National Laboratory's Defense Sciences Engineering Division.

References

1. Poole, B. R., W. C. Ng, C. C. Shang, and G. J. Caporaso (1995), *Wakefield Modeling of Advanced Accelerator Components,* Lawrence Livermore National Laboratory, Livermore, Calif., (UCRL-ID-122235).

2. Ng, K-Y (1988), "Impedances of Stripline Beam-Position Monitors," *Particle Accelerators,* **23**, p. 93.

3. Gluckstern, R. L. (1992), "Coupling Impedance of a Single Hole in a Thick-Wall Beam Pipe," *Phys. Rev. A,* **46**, pp. 1106–1109.

4. Kurennoy, S. S. (1992), "Coupling Impedance of Pumping Holes," *Particle Accelerators,* **39**, pp. 1–13.

TIGER: An Object-Oriented Time-Domain Electromagnetics Simulation Code

David Steich, Jeffrey S. Kallman, J. Brian Grant, Steve Pennock, Niel A. Madsen, Gerald J. Burke, and David J. Mayhall
Engineering Research Division
Electronics Engineering

Brian R. Poole
Defense Sciences Engineering Division
Electronics Engineering

Karl Kunz
The Pennsylvania State University
State College, Pennsylvania

Hal R. Brand and Gary W. Laguna
Computer Applications Sciences and Engineering Division
Computation Organization

The TIGER (from "time domain generalized excitation and response") project began in FY-96. This report provides a description of TIGER's intended performance and the progress we have made.

Introduction

Lawrence Livermore National Laboratory (LLNL) has enjoyed a long history of time-domain leadership in the Computational Electromagnetics (CEM) community, with the development of codes such as AMOS, FDTD, TSAR, TSARLITE, and DSI3D. However, these codes are either research oriented (DSI3D), have limited applicability [AMOS (2.5-D), TSARLITE (2-D)], and/or are no longer regarded as state-of-the-art (TSAR, FDTD). Furthermore, many of these codes have multiple versions that were created over the years for specific applications requiring additional capabilities (such as dispersive TSAR, out-of-core TSAR, dispersive FDTD, near-to-far zone FDTD, advanced boundary condition FDTD, and anisotropic TSARLITE). These codes represent LLNL Engineering's ability to address programmatic time-domain linear electromagnetic modeling needs.

Without exception, all of these codes are extremely difficult to up-grade with the latest technology developments. For example, porting TSAR to a MPP platform, adding required communications to DSI to allow high-order advanced boundary conditions, and modifying AMOS to work for conforming meshes, are all formidable tasks.

At present, the incorporation of new physics into existing codes requires a conscious decision as to which specific code to enhance. Resources are rarely, if ever, available to place enhancements and new physics into several codes. The result is a series of codes with multiple versions built in isolation of one another, making it almost impossible to link them together to provide a larger set of capabilities. The existing problems associated with this collection of CEM codes in LLNL's engineering programs are magnified when difficult simulation requirements demand multiple technology enhancements simultaneously. These limitations will become increasingly debilitating as future modeling requirements become more complex.

In response to these problems, we developed the concept of the TIGER code, an MPP CEM physics kernel that would strengthen LLNL's leadership in linear time-domain CEM technology.

Due to the increasing complexity required to model realistic structures, simultaneous technologies must be suitably applied to reduce the computational burden. **Table 1** shows several such technologies and their potential improvement factors (that is, accuracy, required memory, and/or CPU improvements). Conforming grids eliminate staircasing errors associated with codes such as AMOS, TSAR and FDTD[1].

This improvement in accuracy can be thought of as a reduction in required number of unknowns, since for a given fixed accuracy a coarser grid can be used to represent a given geometry. The drawback is that conforming unstructured nonorthogonal grids often require roughly 30 times the memory overhead, compared to structured orthogonal grids.

However, by using hybrid structured/unstructured grids this high overhead can, to a large extent, be circumvented by judiciously using conforming grids only near appropriate surfaces. Running the code on MPP platforms allows much larger problems to be run much faster than on serial platforms.

Advanced Radiation Boundary Conditions (RBCs) can also reduce the computational effort considerably by allowing the truncation of the problem space to be placed much closer to the scatterer[2]. The actual improvement factors are problem-dependent.

To minimize computational requirements, this full set of technologies must be used simultaneously in a cooperative manner. Simultaneous incorporation of the above technologies in a code that includes advanced materials, physics, interface, and boundary conditions, each with disparate computation and memory requirements, is an ambitious task.

The vision of TIGER extends beyond state-of-the-art modeling of linear time-domain CEM modeling, and includes acoustic wave, elastic wave, and plasma physics modeling capabilities. To help meet the challenges of this task we are collaborating with the EIGER projects at LLNL and Sandia National Laboratories, and the Pennsylvania State University. Each of these collaborators offers much expertise that strengthens the overall effort.

Progress

During the past year we focused our attention on the design of the object-oriented infrastructure that defines the parameter space of the TIGER effort. Object-oriented codes allow flexibility far beyond conventional procedural-based codes. This greatly enhanced flexibility comes at the expense of the extensive up-front design required to build the object-oriented infrastructure. The better the design of the interfaces making up the object-oriented classes, the more flexible the code becomes. A successful design allows new physics capabilities to be included by simple (localized) code additions.

We have built multiple prototype versions of TIGER that test various aspects of the intended performance. We built a FORTRAN 77 quasi-object-oriented version of the code that runs on the CS-2 Meiko and the Cray T3D. This code tested MPI (Message Passing Interface) libraries, simple partitioning algorithms for structured grids, PACT/PANACEA software, and communication overheads associated with algorithms such as the near-to-far zone transformation.

The FORTRAN version works for rectangular structured-grid cells. It was determined that communication overhead for structured grids would be as much of a bottleneck as for unstructured grids even though less information must be communicated between partition boundaries.

Also, it was found that many of the advantages PACT/PANACEA software provides FORTRAN and C-based codes (that is, I/O management, variable dictionaries, and automatic restart capabilities) were not as useful in an object-oriented environment. For example, the need for variable

Table 1. Anticipated performance improvement factors using a given technology enhancement.

Technology enhancement	Improvement factor	Accuracy	Memory	CPU time
Conforming grids	up to 100 ×	√	√	√
Hybrid structured/ unstructured grids	up to 30 ×		√	√
Massively Parallel Processors (MPP)	up to 60 ×		√	√
Advanced Radiation Boundary Conditions (RBC)	up to 20 ×	√	√	√

dictionaries becomes practically obsolete in a C++ language that allows extensive information hiding and name space capabilities.

Also, at this time the PACT/PANACEA software does not support C++. For these reasons we decided not to pursue using PACT/PANACEA within the TIGER code. However, in the future we intend to interface with data and codes that use PACT/PANACEA software by providing filters that can translate to the PACT/PANACEA format.

Other prototype C++ versions of TIGER tested primarily the mesh management systems required to insulate the physics from the bookkeeping. Insulation of the physics from mesh-specific operations is the key factor in the extensibility, flexibility, and maintainability of the code.

Much effort during the past year has also been expended on issues of memory and execution time efficiency. A major goal of the TIGER project is to have overhead as close as possible to that of existing codes which are specialized for specific algorithms. In the past, object-oriented codes were not able to compete with "hand-coded" optimized FORTRAN or C codes. However, with the use of template expressions and traits[3,4] a fully objected-oriented C++ code can perform within a few percent of hand-coded software.

This year we also up-graded the Anastasia mesh generation package to allow BRLCAD (a popular army CAD/CAM code) solid models to be meshed in terms of rectangular brick elements. The modification of Anastasia will allow us to meet some short term deliverables. A much more sophisticated mesh generator will soon be required as TIGER becomes more functional.

Object-Oriented Approach

The object-oriented infrastructure we have begun building this year is shown in **Fig. 1**. The figure shows six management systems that will be built to insulate the core physics algorithms from the rest of the code, thus freeing physics programmers from having to worry about:

1) what type of mesh their algorithm will be applied to (mesh management);
2) whether the code will be run serial, parallel distributed, or shared (communication management);
3) the allocating and freeing of memory (memory management);
4) how to read in, store, and write out information (I/O management);
5) whether the user is attempting illegal tasks (parameter and constraint management); and
6) how to manage input parameters, runs, results, projects (database management).

Providing an object-oriented framework with long-term extensibility for each of these management systems will be accomplished by an emphasis on isolating concepts and their fundamental relationships. On the surface, this sounds insignificant but in actuality it is the key to extending the shelf-life of an object-oriented program.

A small portion of the mesh management system is displayed in **Fig. 1**. The mesh management abstraction allows different kinds of meshes to be used in an identical way by providing a common mesh interface that hides details. The structured mesh database that exists behind the interface consists of a series of functions, while the unstructured mesh database consists of a complex set of memory index arrays.

In numerical analysis, discretized equations are often used to approximate the actual equations. In TIGER's object-oriented approach, discretized operators are used to build these discretized equations (see lower portion of **Fig. 1**) that simulate the physics. In this way, equations can be thought of as a collection of operators applied to field quantities. These discretized operators manipulate field quantities that lie on the numerical mesh.

Manipulation of fields by these operators occurs through the mesh interface and allows the same operators to be used independent of mesh type. The mesh management system is a vital part of the overall TIGER effort, and has been the primary focus of our efforts this year. A major portion of this management system has been completed.

The memory management system organizes memory-specific allocations and deallocations in an efficient manner. Often in object-oriented codes the getting and freeing of memory can be a major portion of the overall execution time. This interaction with the operating system can degrade performance compared to "hard-wired" FORTRAN or C-based codes. Our memory management system grabs large blocks of memory from the system and dispenses required chunks of memory efficiently. A rudimentary memory management system has been built this year.

We have also begun work on the communication and parameter/constraint management systems as well. The I/O and database management systems are future tasks that will become important as TIGER becomes more functional.

The object-oriented operator-based approach of TIGER not only makes the code easily extensible and maintainable but also provides flexibility far beyond the conventional procedural approach. For example,

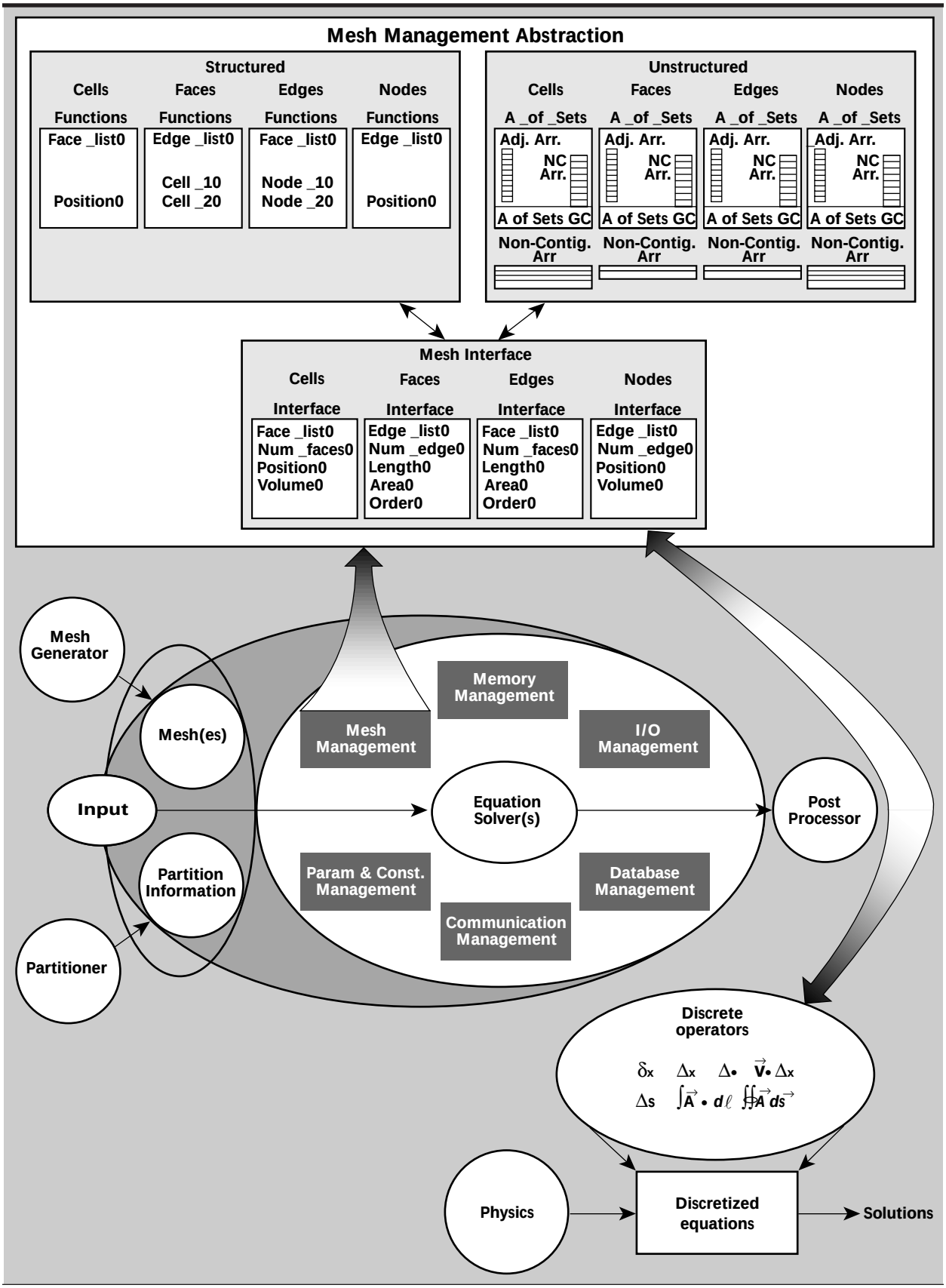

Figure 1. Insulating generalized physics from bookkeeping.

consider the implementation of RBCs, which are required to truncate the numerical mesh for all open scattering problems.

A pictorial representation of a procedural versus object-oriented approach is shown in **Fig. 2**. To write a code containing many possible RBCs which could be applied to many different mesh types typically would require the product of (# of RBCs) × (# of mesh types) implementations (see top portion of **Fig. 2**).

Using an object-oriented approach, the mesh and RBC equations can both be abstracted (see bottom portion of **Fig. 2**). A single implementation can then be constructed using the mesh interface and the abstracted set of operators to obtain the appropriate set of operations. The single "operator-based" equation is more complicated to write than one of the "procedural-based" equations, but the same implementation works for almost every mesh type and RBC type which can be cast into the abstracted forms (factors such as numerical stability, numerical dispersion, and stencil size may prohibit certain implementations). The key is to have the abstractions be as general as possible to encompass the largest set of capabilities. Progress on these abstractions is underway and is at the heart of the TIGER effort.

The mesh management system is responsible for the grid abstractions (**Fig. 3**). A very small subset of RBC types is shown on the left-hand side of **Fig. 3**. Each RBC type has multiple orders and variations resulting in a plethora of possible RBC equations. Shown near the center of **Fig. 3** is a blow-up of a third-order Higdon boundary condition. Inside the matrix are 64 terms, with each term having a dozen or so sub-terms. Other more complicated boundary conditions require 4-D matrices involving hundreds of terms to describe the RBCs' coefficients. Shown in the lower portion of **Fig. 3** are simple operators **A**, **B**, **C**, that have been abstracted out of the RBC equations along with some operations that can be used with the operators, such as +, - , dot product, inverse.

Also shown in the lower portion of **Fig. 3** is the same third-order Higdon boundary condition written in terms of these operators. Note the significant reduction in the complexity of equation representation. The expression is exactly identical to the expression shown in the upper portion of **Fig. 3**. The approach is very general and even allows new boundary conditions to be invented simply by defining new operators or by concatenating them together (that is, a Liao-Higdon-Mur RBC).

The end result is a powerful technique that can greatly increase accuracy and reduce execution times required to solve problems. Shown on the right-hand side of **Fig. 3** are a second-order Mur and a third-order Taylor RBC. Shown are the results of a convergence study testing the number of cells required before a converged solution is obtained.

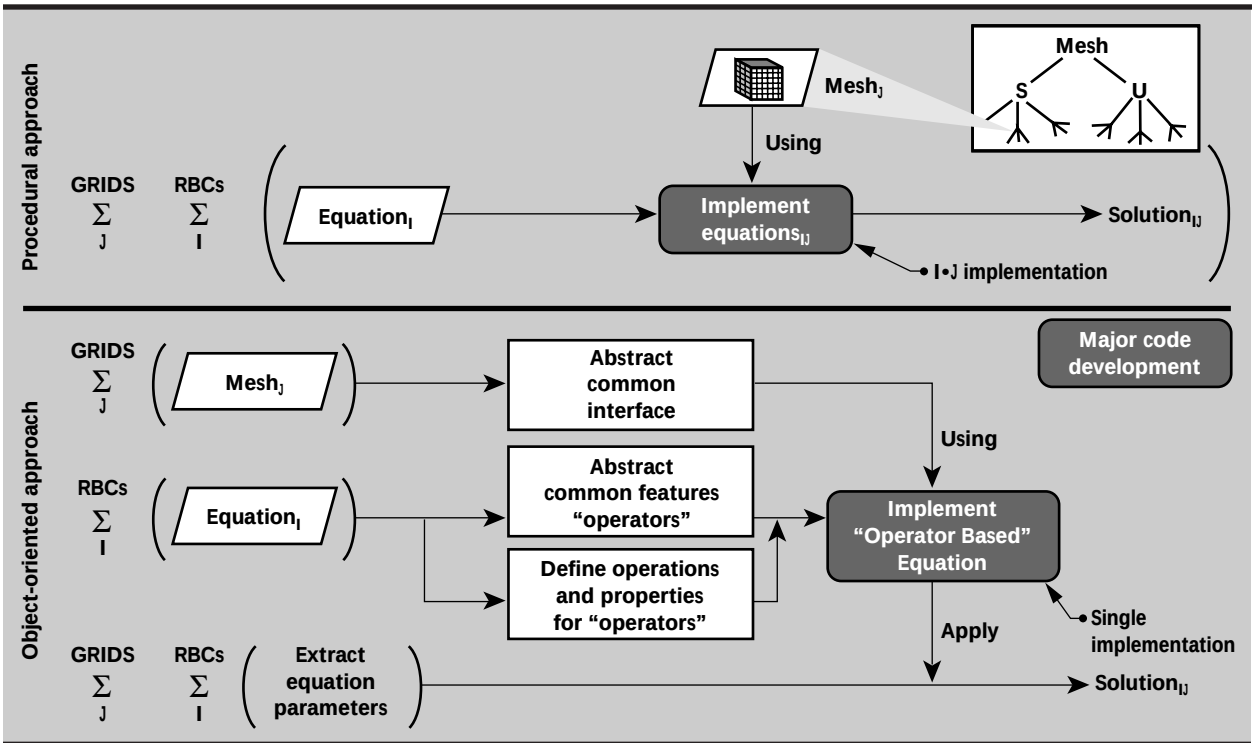

Figure 2. RBCs: Procedural versus object-oriented approach.

It is obvious that the Taylor boundary condition is fully converged already, using 80,000 cells. The Mur RBC, perhaps the most popular boundary condition used over the past 15 years, has still not converged, even after using over 1.2 million cells. The Taylor boundary condition was invented using the operator abstractions described above. We now have the capability to represent literally hundreds of RBCs using this research. We can model virtually every local RBC in the community today simply by changing parameters used to initialize the operators. (A new boundary condition called the Perfectly Matched Layer (PML) requires a slightly different set of operators but still fits into the above described approach.)

This operator-based approach to RBCs is cutting-edge technology, unique in the world.

Future Work

The focus of our collaborative efforts for FY-97 will be to continue to build the objected-oriented management class infrastructures that provide the required insulation between the physics and the bookkeeping. Specifically, the essential parts of the mesh, communication, and memory management systems are expected to be in place in FY-97. The mesh management system will eventually allow numerous mesh types (such as structured, unstructured, expanding, uniform, 2-D, 3-D, skewed, and nonorthogonal) to be abstracted into a common interface.

The communication management system will organize processor topologies, sending and receiving of data, and execution barriers required for shared

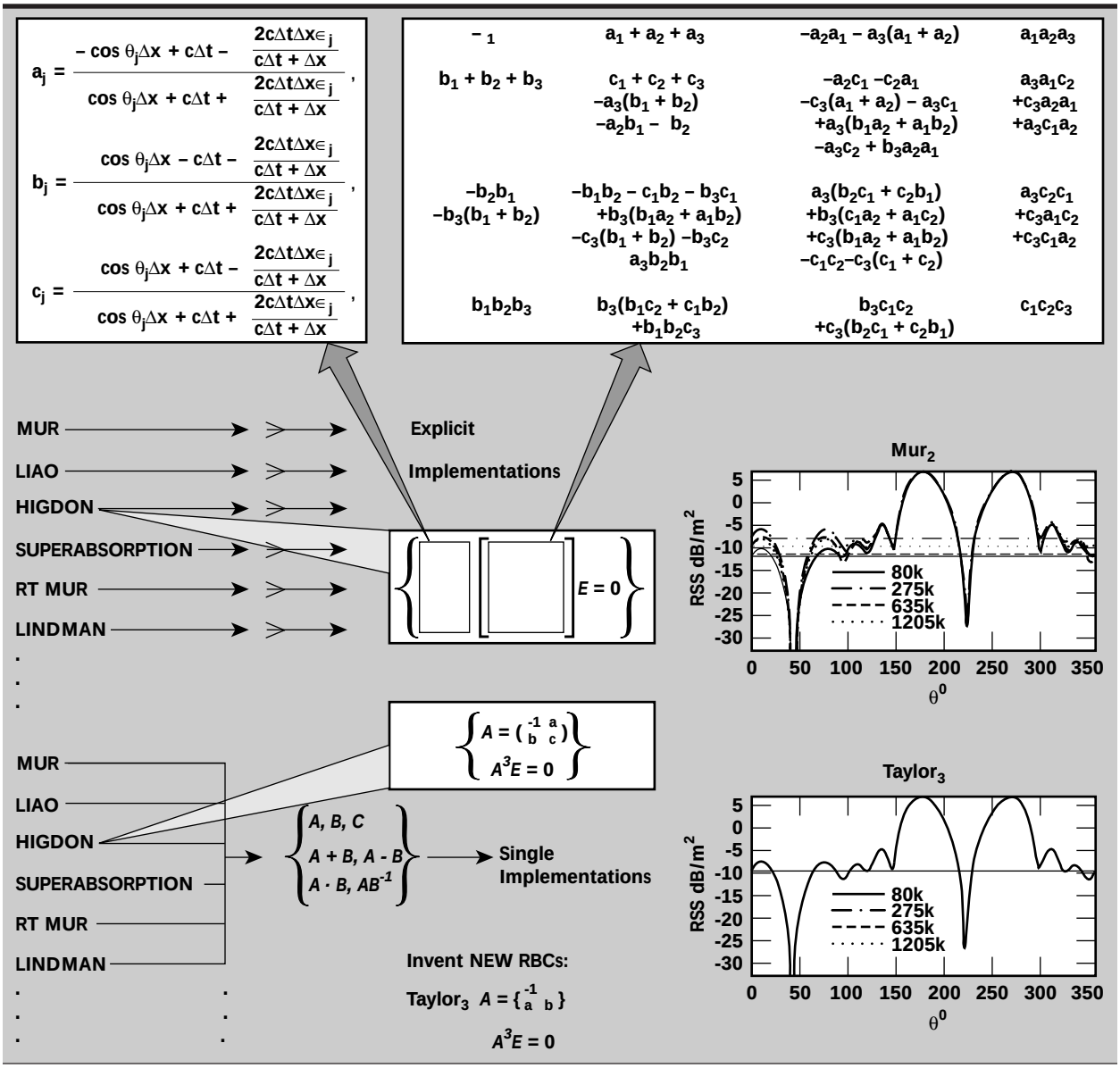

Figure 3. Operator-based approach to RBCs.

and distributed memory multiprocessor computer architectures. We will also continue building physics modules that use these management systems.

We will also research issues required for the simultaneous implementation of the technology enhancements shown in **Table 1**. The research areas are:

1) an efficient hybrid grid realization;
2) generalized advanced material algorithms for hybrid grids;
3) generalization of algorithms at grid interfaces that enforce conservation laws;
4) efficient MPP communication in the presence of these generalizations; and
5) efficient MPP load-balancing for hybrid grids.

In addition to the above research topics, we will develop the following new physics:

1) wakefield calculations for arbitrary beampipe cross sections;
2) advanced RBCs in the presence of Perfect Electrical Conductors (PEC);
3) advanced RBCs in the presence of complex sources;
4) advanced material modeling formulations for nonorthogonal grids; and
5) the simulation of a curved beamline source for complex geometries on hybrid grids.

We anticipate that TIGER will quickly surpass all of LLNL Engineering's linear time-domain EM code capability by the end of FY-97.

The first major use of the TIGER code will be in the modeling and design of accelerator and electron beam transport components for the Advanced Hydrotest Facility (AHF) which will be a major part of the Science Based Stockpile Stewardship (SBSS) Program. In AHF, a linear induction accelerator generates a high-current, relativistic electron beam for the generation of x rays for use in pulsed radiography applications. **Figure 4** is an illustration of the AHF facility with key accelerator components that will be modeled by the TIGER code.

Of prime importance in the design of high-current electron beam accelerator and beam transport systems is the understanding and control of the scattered electromagnetic fields associated with the passage of a relativistic electron beam through the system. These scattered electromagnetic fields are referred to as wakefields. The wakefields can lead to degradation of the beam with the resultant loss of beam quality at the target, or worse, can lead to beam breakup instabilities with total loss of beam transport.

Excellent results have been achieved with TSAR for the modeling of wakefields in 3-D structures (see "Three-Dimensional Electromagnetic Modeling of Wakefields in Accelerator Components," a separate report in this thrust area.) However, the full scale

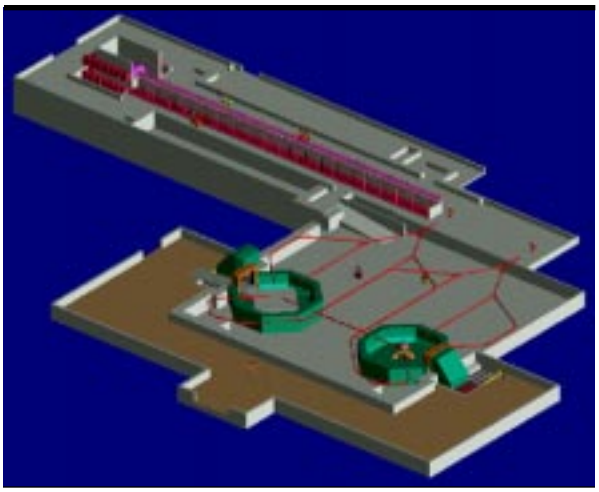

Figure 4. AHF facility, with four critical accelerator components that will be modeled with TIGER.

models will require a more robust code. Full 3-D modeling of complex structures has been limited due to the substantial computer resources required for a fully 3-D model. This is particularly true with TSAR, where its cubical cell-structured mesh significantly limits the development of realistic models. Development of TIGER using conforming unstructured meshes will allow a substantial increase in the geometric fidelity of the structures being modeled and, with its advanced boundary conditions, will allow a more realistic truncation of the computational problem space.

Acknowledgments

The authors acknowledge the assistance of the EIGER Project staff at both LLNL and Sandia National Laboratories.

We would also like to thank C. Shang for his strong support of this project.

References

1. Madsen, N. K. (1995), "Divergence Preserving Discrete Surface Integral Methods for Maxwell's Curl Equations Using Non-Orthogonal Unstructured Grids," *J. Comput. Physics,* Vol. **119**, (1), June, pp. 34-45.

2. Steich, D. J. (1995), "Local Outer Radiating Boundary Conditions for the Finite-Difference Time-Domain Method Applied to Maxwell's Equations," Ph.D. dissertation, Pennsylvania State University.

3. Veldhuizen, T. (1995), "Expression Templates," *C++ Report Magazine*, Vol. **7**, (5), June.

4. Myers, N. (1995), "A New and Useful Template Technique: 'Traits'," *C++ Report Magazine*, Vol. **7**, (5), June.

Anisotropic Magnetic and Electric Material Models in Computational Electromagnetic Codes

Scott D. Nelson
Defense Sciences Engineering Division
Electronics Engineering

Gerald J. Burke and David J. Steich
Engineering Research Division
Electronics Engineering

We have demonstrated that the recursive-convolution solution for anisotropic and dispersive media yields accurate results for reflection from ferrite and plasma slabs up to a frequency limit set by the sampling interval. Several different forms of the up-date equations were considered which can result from different approximations in reducing the continuous equations to discrete forms.

Introduction

Magnetic and electric tensor material characteristics are central to a broad class of complex materials such as plasmas and crystals. Many devices in electromagnetics use external fields to bias a ferrite material or an electro-optic material. This bias then changes the field propagation characteristics, based on the direction of travel through the medium with respect to the direction of the applied field. The incorporation of anisotropic materials into Lawrence Livermore National Laboratory (LLNL)'s computational electromagnetic design codes allows for the expansion into these areas.

In recent years the finite-difference time-domain (FDTD) solution procedure developed by K. S. Yee has been extended to dispersive and anisotropic media to handle materials such as magnetized ferrites and plasmas. The constitutive relations for the dispersive material can be introduced into the solution through either a convolution integral or a differential equation. We have examined the convolution form, which uses a recursive update procedure, for use in design codes under development at LLNL.

The coupling of field components in anisotropic media can result in a substantial increase in complexity and evaluation time for the computational electromagnetic update equations. However, we note that the equations simplify greatly if the impulse response of the susceptibility is zero at time equal to zero, as is true of some materials. Some variations in the basic up-date equations, resulting from the approximations in going from continuous to discrete form, were examined, and results were compared for accuracy and stability.

A 3-D code was written to test these solutions, but was validated for the 1-D problem of reflection and transmission by a magnetized ferrite or plasma slab, since the exact reflection and transmission coefficients are available for this problem.

Progress

Material Formulation for Gyrotropic Media

The case of anisotropic and dispersive magnetic material will be used here as an example. The magnetic field up-date equation for such material is obtained by combining the Maxwell's equation

$$\frac{\partial \mathbf{B}}{\partial t} = -\nabla \times \mathbf{E} \tag{1}$$

and the equation relating **B** and **H** in convolution form

$$\mathbf{B}(t) = \mu_o \left[\mathbf{H}(t) + \int_o^t \overline{\overline{\chi}}_m (t-\tau) \cdot \mathbf{H}(\tau) d\tau \right] \tag{2}$$

where $\bar{\bar{\chi}}_m(t)$ is the susceptibility tensor representing the impulse response of the material. To eliminate **B** from **Eq. 1** the derivative of **Eq. 2** can be evaluated as

$$\frac{\partial}{\partial t}\mathbf{B}(t) = \mu_o\left[\frac{\partial}{\partial t}\mathbf{H}(t) + \bar{\bar{\chi}}(t)\cdot\mathbf{H}(0) + \int_o^t \bar{\bar{\chi}}(\tau)\cdot\frac{\partial}{\partial t}\mathbf{H}(t-\tau)d\tau\right] \tag{3}$$

or as

$$\frac{\partial}{\partial t}\mathbf{B}(t) = \mu_o\left[\frac{\partial}{\partial t}\mathbf{H}(t) + \bar{\bar{\chi}}(0)\cdot\mathbf{H}(t) + \int_o^t \frac{d}{dt}\bar{\bar{\chi}}(t-\tau)\cdot\mathbf{H}(\tau)d\tau\right]. \tag{4}$$

Converting **Eq. 3** to discrete form with a pulse approximation of the integral leads to the magnetic field up-date equation

$$\mathbf{H}^{n+1/2} = \left[\bar{\bar{\mathbf{I}}} + \frac{\Delta t}{2}\bar{\bar{\chi}}_m(0)\right]^{-1}\left[\bar{\bar{\mathbf{I}}} - \frac{\Delta t}{2}\bar{\bar{\chi}}_m(0)\right]\cdot\mathbf{H}^{n-1/2} - \Delta t\left[\bar{\bar{\mathbf{I}}} + \frac{\Delta t}{2}\bar{\bar{\chi}}_m(0)\right]^{-1}\cdot\Psi^n - \frac{\Delta t}{\mu_o}\left[\bar{\bar{\mathbf{I}}} + \frac{\Delta t}{2}\bar{\bar{\chi}}_m(0)\right]^{-1}\cdot\nabla\times\mathbf{E}^n \tag{5}$$

where

$$\Psi^n = \sum_{i=0}^{n-1}\left[\bar{\bar{\chi}}_m\left[(n-i)\Delta t\right] - \bar{\bar{\chi}}_m\left[(n-i-1)\Delta t\right]\cdot\mathbf{H}^{i+1/2}\right].$$

Starting with **Eq. 4** and representing $\partial\boldsymbol{H}(t)/\partial t$ with a central difference and $\mathbf{H}(t)$ with an average from times $(n - 1/2)\Delta t$ and $(n + 1/2)\Delta t$ leads to an equation similar to **Eq. 5**, but with Ψ^n replaced by $\Delta t\Psi'^n$ where

$$\Psi'^n = \sum_{i=0}^{n-1}\bar{\bar{\chi}}'_m\left[\left(n-i-\tfrac{1}{2}\right)\Delta t\right]\cdot\mathbf{H}^{i+1/2}.$$

Somewhat different results can be obtained for **Eq. 5** from different interpretations of the pulse approximation of the integral, or in the equation derived from **Eq. 4** by using the value at the forward time step rather than the average for $\mathbf{H}(n\Delta t)$. In fact, adding the same small quantity to both square-bracketed terms results in a second-order change in the product multiplying $\mathbf{H}^{n-1/2}$. Hence **Eq. 5** can be reduced to

$$\mathbf{H}^{n+1/2} = \left[\bar{\bar{\mathbf{I}}} + \Delta t\bar{\bar{\chi}}_m(0)\right]^{-1}\cdot\left(\mathbf{H}^{n-1/2} - \Delta t\,\Psi^n - \frac{\Delta t}{\mu_o}\nabla\times\mathbf{E}^n\right) \tag{6}$$

by adding $(\Delta t/2)\bar{\bar{\chi}}(0)$ to both coefficients, or by subtracting the same quantity

$$\mathbf{H}^{n+1/2} = \left[\bar{\bar{\mathbf{I}}} - \Delta t\bar{\bar{\chi}}_m(0)\right]\cdot\mathbf{H}^{n-1/2} - \Delta t\,\Psi^n - \frac{\Delta t}{\mu_o}\nabla\times\mathbf{E}^n. \tag{7}$$

When $\bar{\bar{\chi}}(0) = 0$, which occurs in materials such as Lorentz dielectrics, **Eqs. 5, 6,** and **7** all reduce to the simpler and easier to use form

$$\mathbf{H}^{n+1/2} = \mathbf{H}^{n-1/2} - \Delta t\Psi^n - \frac{\Delta t}{\mu_o}\nabla\times\mathbf{E}^n. \tag{8}$$

The evaluation of a single vector component of the product of a tensor with the curl of the field can involve 36 field values. However, this can be reduced to 20 values by combining and canceling terms. When the elements of $\bar{\bar{\chi}}(t)$ are represented as sums of exponentials Ψ^n can be evaluated from Ψ^{n-1} through a simple recursion relation, although additional averaging is needed for anisotropic media.

The results of solving **Eq. 5** for a pulse normally incident on a ferrite slab are shown in **Fig. 1**.

The magnitudes of the reflection and transmission coefficients for right-hand circular polarization are compared with the exact results, and the relative errors in the complex quantities are also shown. The relative errors from solving **Eqs. 5, 6,** and **7** are compared in **Fig. 2**.

While the differences in error are fairly small, **Eq. 5** appears to be more stable near the Courant limit, as shown by the comparison with **Eq. 6** in **Fig. 3**.

Equation 6 continued to show greater instability at late time when Δt was reduced to $\Delta x/c\sqrt{3}$, while **Eq. 5** showed no significant instability at this time increment. The stability of **Eq. 7** was similar to that of **Eq. 6**.

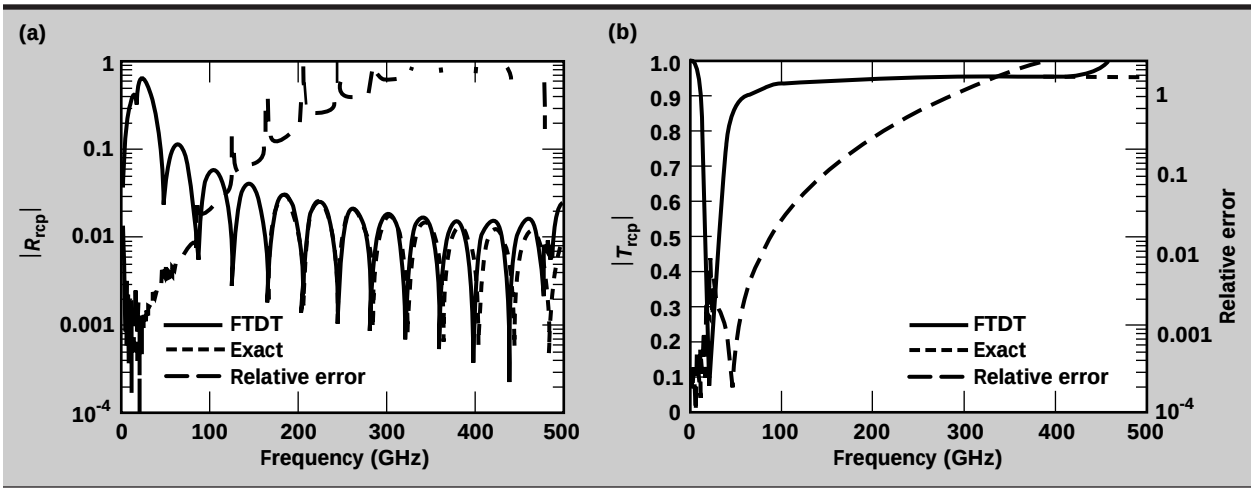

Figure 1. Magnitudes of the reflection (a) and transmission (b) coefficients for normal incidence on a ferrite slab from the FDTD solution, compared with the exact solutions. The relative errors in the complex quantities are also shown.

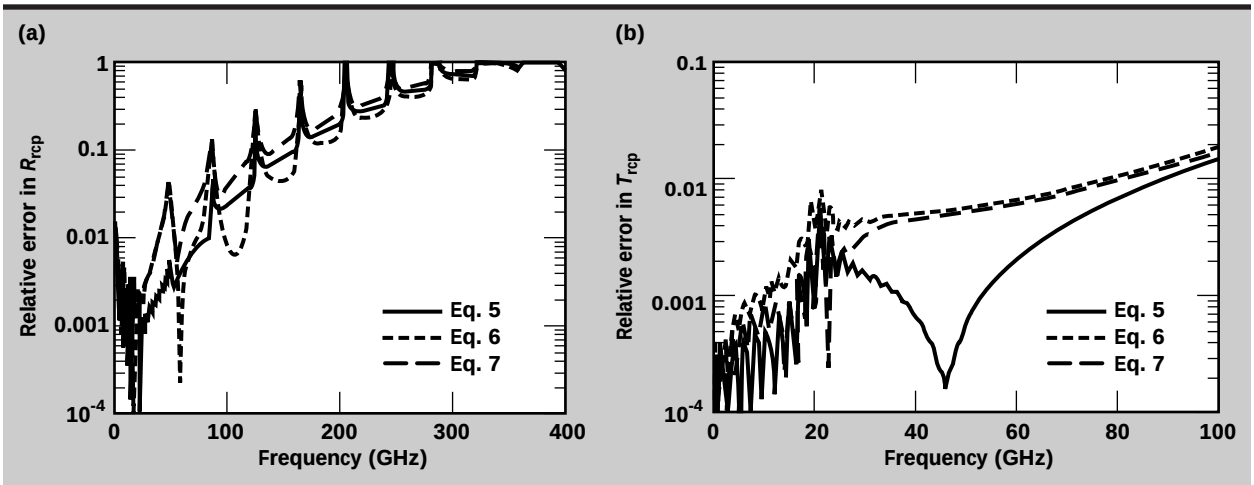

Figure 2. Relative errors in the complex reflection (a) and transmission (b) coefficients from solving Eqs. 5, 6, and 7 for normal incidence on a ferrite slab with $\Delta t = \Delta x / 2c\sqrt{3}$.

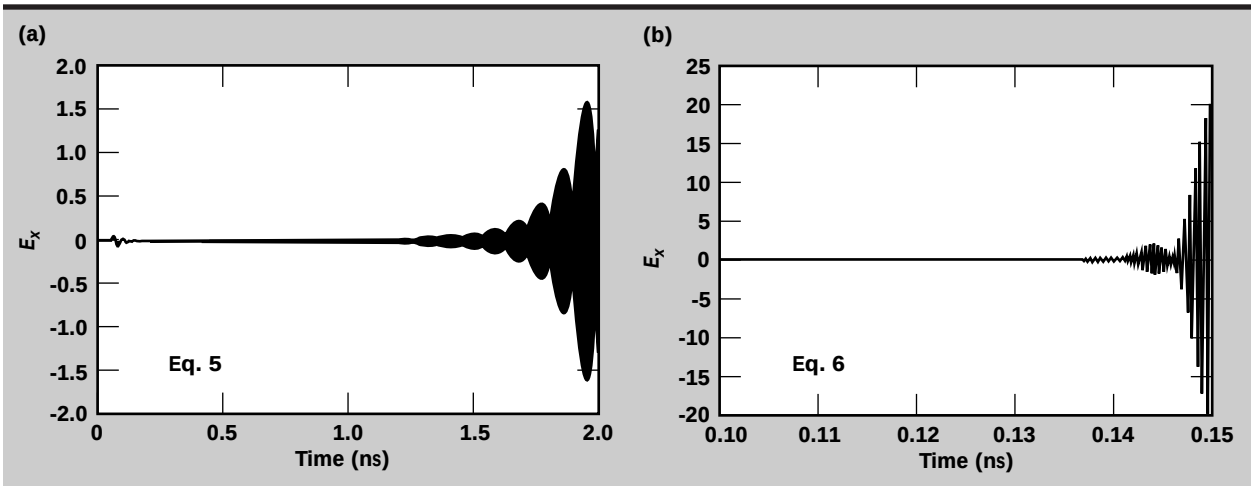

Figure 3. Electric field in front of the ferrite slab, showing instability of Eqs. 5 and 6 solved at the 1-D Courant limit of $\Delta t = \Delta x/c$.

Non-Dispersive Anisotropic Media

For a simple non-dispersive anisotropic medium ε_r and μ_r become constant tensors, so that the constitutive relations are

$$\mathbf{D} = \varepsilon_o \bar{\bar{\varepsilon}}_r \cdot \mathbf{E} = \varepsilon_o \begin{pmatrix} \varepsilon_{11} & \varepsilon_{12} & \varepsilon_{13} \\ \varepsilon_{21} & \varepsilon_{22} & \varepsilon_{23} \\ \varepsilon_{31} & \varepsilon_{32} & \varepsilon_{33} \end{pmatrix} \begin{pmatrix} E_x \\ E_y \\ E_z \end{pmatrix} \tag{9}$$

$$\mathbf{B} = \mu_o \bar{\bar{\mu}}_r \cdot \mathbf{H} = \mu_o \begin{pmatrix} \mu_{11} & \mu_{12} & \mu_{13} \\ \mu_{21} & \mu_{22} & \mu_{23} \\ \mu_{31} & \mu_{32} & \mu_{33} \end{pmatrix} \begin{pmatrix} H_x \\ H_y \\ H_z \end{pmatrix} \tag{10}$$

Substituting **Eqs. 9** and **10** into the basic up-date equations for **B** and **D**, the up-dated fields are obtained in terms of the inverses of the $\bar{\bar{\varepsilon}}_r$ and $\bar{\bar{\mu}}_r$ tensors as

$$\mathbf{H}^{n+1/2}(i,j,k) = \mathbf{H}^{n-1/2}(i,j,k) - (\Delta t/\mu_o)\bar{\bar{\mu}}_r^{-1} \cdot \nabla \times \mathbf{E}^n(i,j,k) \tag{11}$$

and

$$\mathbf{E}^{n+1}(i,j,k) = \mathbf{E}^n(i,j,k) + (\Delta t/\varepsilon_o)\bar{\bar{\varepsilon}}_r^{-1} \cdot \nabla \times \mathbf{H}^{n+1/2}(i,j,k). \tag{12}$$

The components of the vector equations **Eqs. 11** and **12** are still evaluated at the off-set locations of the Yee cell. However, the dot product requires all vector components of the curl at each location. The components that are not directly available from the central difference formulas must be obtained by averaging. The equation for $H_x\left(i, j+\frac{1}{2}, k+\frac{1}{2}\right)$ is

$$H_x^{n+1/2} = H_x^{n-1/2} - \frac{\Delta t}{\mu_o}\begin{bmatrix} \mu_{11}^{-1}\left(\nabla \times \mathbf{E}^n\right)_x \\ +\mu_{12}^{-1} A_{xy}^H\left[\left(\nabla \times \mathbf{E}^n\right)_y\right] \\ +\mu_{13}^{-1} A_{xz}^H\left[\left(\nabla \times \mathbf{E}^n\right)_z\right] \end{bmatrix}$$

while

$H_y\left(i+\frac{1}{2}, j, k+\frac{1}{2}\right)$ is

$$H_y^{n+1/2} = H_y^{n-1/2} - \frac{\Delta t}{\mu_o}\begin{bmatrix} \mu_{21}^{-1} A_{yx}^H\left[\left(\nabla \times \mathbf{E}^n\right)_x\right] \\ +\mu_{22}^{-1}\left(\nabla \times \mathbf{E}^n\right)_y \\ +\mu_{23}^{-1} A_{yz}^H\left[\left(\nabla \times \mathbf{E}^n\right)_z\right] \end{bmatrix}$$

and

$H_z\left(i+\frac{1}{2}, j+\frac{1}{2}, k\right)$ is

$$H_z^{n+1/2} = H_z^{n-1/2} - \frac{\Delta t}{\mu_o}\begin{bmatrix} \mu_{31}^{-1} A_{zx}^H\left[\left(\nabla \times \mathbf{E}^n\right)_x\right] \\ +\mu_{32}^{-1} A_{zy}^H\left[\left(\nabla \times \mathbf{E}^n\right)_y\right] \\ +\mu_{33}^{-1}\left(\nabla \times \mathbf{E}^n\right)_z \end{bmatrix}$$

where A_{xy}^H yields a value of the argument at the H_x location by averaging from four surrounding H_y positions. The averaging for all components of the curl at a single location involves 36 field values. However, eight of these cancel and another eight can be combined in the dot product of the curl with a vector, leaving 20 unique field values. The complete result for a product such as $\bar{\bar{\mu}}_r^{-1} \cdot \nabla \times \mathbf{E}$, with each component of the resulting vector located at the correct Yee-cell location, can be obtained from a total of 36 unique values of **E**, since each value is used more than once. This compares with 108 if no attempt is made to cancel or reuse values.

Results

The solution for gyrotropic media was validated for a plane wave normally incident on a ferrite slab with the biasing magnetic field in the direction of propagation, along the z axis. This problem was chosen because the reflection and transmission coefficients for the slab are available in simple analytic form. In this case, a 3-D code was written, using the equations from the preceding section. Since the plane wave propagating through the ferrite in the direction of the biasing field splits into right-hand and left-hand circularly polarized waves with different propagation constants, the problem space was terminated in even-symmetry boundary conditions in both x and y boundary planes. First-order Mur boundary

conditions were used at the z boundaries, but for the results shown here the z extent of the problem space was made large enough to gate out the reflections, thus eliminating the boundary conditions as a source of error.

For the ferrite, biased with magnetic field along the z axis, the relative permeability tensor at a frequency ω is

$$\bar{\bar{\mu}}_r(\omega) = \begin{pmatrix} \mu(\omega) & jk(\omega) & 0 \\ -jk(\omega) & \mu(\omega) & 0 \\ 0 & 0 & 1 \end{pmatrix} = \begin{pmatrix} 1+\chi_{11}(\omega) & \chi_{12}(\omega) & 0 \\ \chi_{21}(\omega) & 1+\chi_{22}(\omega) & 0 \\ 0 & 0 & 1 \end{pmatrix}$$

where

$$\chi_{11}(\omega) = \chi_{22}(\omega) = \frac{(\omega_o + j\omega\alpha)\omega_m}{(\omega_o + j\omega\alpha)^2 - \omega^2}$$

$$\chi_{12}(\omega) = -\chi_{21}(\omega) = \frac{j\omega\omega_m}{(\omega_o + j\omega\alpha)^2 - \omega^2}.$$

The parameters of the ferrite modeled here were

$$\omega_o = (2\pi)\cdot 20\times 10^9\, rad/s$$
$$\omega_m = (2\pi)\cdot 10\times 10^9\, rad/s$$
$$\alpha = 0.1$$

Results for this ferrite with $\Delta x = 75(10^{-6})m$ and $\Delta t = \Delta x/(2c\sqrt{3})$ with 6000 time steps are shown in **Fig. 1**. The source was a Gaussian-pulse plane wave with full-width-half-max equal to 0.001 m. Since the solution is uniform in the x and y directions the problem was solved with 3 cells in x and y and 4000 cells in z, to eliminate the radiating boundaries, and the ferrite filled 50 cells for a thickness of 0.00375 m.

Conclusions

The recursive-convolution solution for anisotropic and dispersive media was seen to yield accurate results for reflection from ferrite and plasma slabs up to a frequency limit set by the sampling interval. Depending on the application, the results shown might be considered usable up to about 300 GHz, which corresponds to about 13 cells per wavelength. Results at still higher frequencies might be usable when a time delay or frequency shift due to dispersion can be tolerated. The deconvolved results became unstable not far beyond the upper limits of the plots.

The main difficulties in implementing the solution for anisotropic and dispersive media are evaluating the product of a tensor with the curl of a field, and the tensor multiplying the previous values of the field that is being up-dated. The number of values needed in evaluating the product with the curl can be reduced by combining and canceling terms, but that can restrict generality of a code in the treatment of mesh types. The product of a tensor with the field being up-dated presents bookkeeping problems that can be circumvented, at the expense of added storage, by computing the new values in a separate array.

Several different forms of the up-date equations were considered which can result from different approximations in reducing the continuous equations to discrete form.

Nodular Defect-Induced Field Enhancements in High-Power Multilayer Optical Coatings

Nicole E. Molau and Clifford C. Shang
Engineering Research Division
Electronics Engineering

Hal R. Brand
Computer Applications Sciences and Engineering Division
Computations Organization

Mark R. Kozlowski
Inertial Confinement Fusion
Laser Programs

In FY-96, we completed the 2-1/2-D electromagnetic modeling of rotationally-symmetric nodular defect geometries in high-power optical high-reflectance coatings.

Introduction

Advances in the design and production of high damage threshold optical coatings for use in mirrors and polarizers have been driven by the design requirements of high-power laser systems such as the proposed 1.8-MJ National Ignition Facility (NIF) and the prototype 12-kJ Beamlet laser system at Lawrence Livermore National Laboratory (LLNL). The present design of the NIF will include 192 polarizers and more than 1100 mirrors. Currently, the material system of choice for high-power multilayer optical coatings with high damage threshold applications near 1.06 μm is e-beam deposited HfO_2/SiO_2 coatings. However, the optical performance and laser damage thresholds of these coatings are limited by micron-scale defects and insufficient control over layer thickness.

In multilayer dielectric stack mirrors, the predominant surface defects are micron-scale domes associated with the classic nodule defect. These defects are initiated at seed particles that are either present on the substrate or deposited during the film deposition process. The seed particles can arise from several sources: contamination within the vacuum system, substrate contamination, or particles ejected from the coating source material itself. Nodular defects are produced during film deposition as a result of shadowing effects at seed particles during the growth process. These defects give rise to local electric field enhancements which lead to "hot spots" in the coatings since the heat generation is proportional to the square of the electric field, and these rapidly expanding regions create tensile stresses which may result in mechanical failure of the coatings.

In FY-96, we completed the 2-1/2-D electromagnetic (EM) modeling of rotationally-symmetric nodular defect geometries in high-power high-reflectance (HR) optical coatings. Twenty-three different defect geometries were studied to investigate the influence of nodule size, depth, and material composition on electric field enhancements within the structure.[1,2] The heat generation rates for these defect geometries were computed based on the EM simulations and coupled into the thermal-mechanical model for each geometry.[2] This report will summarize the 2-1/2-D EM modeling results; the thermal-mechanical modeling results are reported elsewhere.[3]

Progress

In FY-96 we completed the 2-1/2-D EM modeling (assuming normal-incidence illumination) of 23 different rotationally-symmetric nodular defect geometries similar to that shown schematically in **Fig. 1**. The 2-1/2-D finite-difference time-domain (FDTD) EM code, AMOS[4,5] was used to calculate the steady-state electric field profiles throughout each rotationally-symmetric defect geometry, by solving

the Maxwell equations and applying the appropriate boundary conditions[6] and material models. AMOS generates a 2-D solution in the r-z plane and assumes an explicit ϕ-variation to achieve the full 3-D solution for the rotationally-symmetric object.

These steady-state electric field profiles were used to calculate the heat generation distribution (σE^2 in W/m^3 with σ, the electrical conductivity in S/m and E, the steady-state electric field in V/m) throughout each geometry. This heat generation distribution was then coupled into the thermal-mechanical model as the initial conditions, resulting in a full electro-mechanical model of nodule failure.

The steady-state electric field profile everywhere within a 2-D r-z cross-section (for $\phi = 0^\circ$) of a typical nodular defect geometry is shown in **Fig. 2**. In this case, the nodular defect geometry consists of a spherical HfO_2 seed of diameter, d = 0.73 μm; depth, T = 1.97 μm; and nodule dome diameter, D = 3.392 μm. The source was assumed to be a normally-incident, sinusoidally-varying, linearly-polarized, plane wave (λ_o = 1.06 μm) with an average input power density of 1 GW/cm^2. As is illustrated in **Fig. 2**, for rotationally-symmetric nodular defect geometries under normal-incidence illumination, the peak electric fields and highest electric field enhancements are typically located along the axis of symmetry.

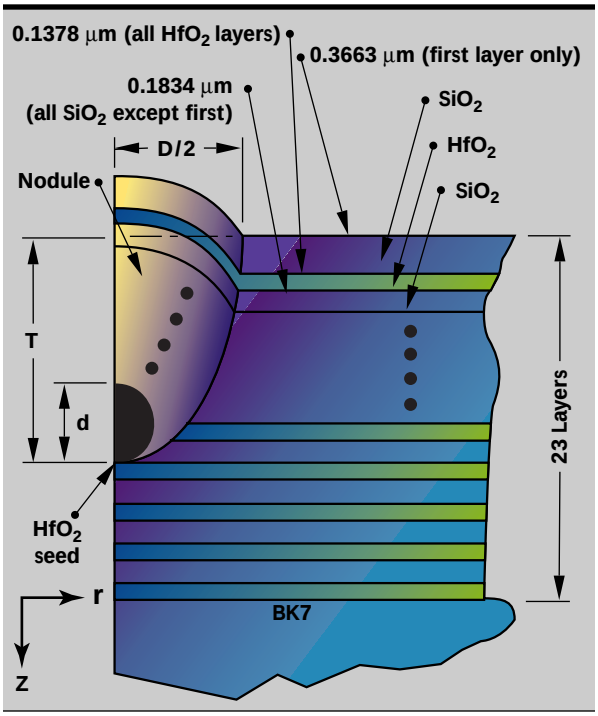

*Figure 1. 2-D cross-sectional schematic of a typical rotationally-symmetric nodular defect geometry containing a seed of diameter, d, embedded some depth, T, into the HR stack, with parabolic sides defined by the relation, D = (8*T*d)$^{1/2}$.*

The electric field standing wave (EFSW) pattern along the axis of symmetry (r = 0 μm) of the nodule and the EFSW pattern along a line parallel to the axis of symmetry but at a radius of 5 μm are also shown in **Fig. 2**. The EFSW pattern along the axis of symmetry shows several localized electric field enhancements within the HR coating, one in the SiO_2 overcoat and one in the HfO_2 seed, while the EFSW pattern for the line at r = 5 μm looks very much like that of the perfect HR stack.

This is to be expected since, for radii larger than the defect dome radius, D/2 = 1.696 μm, the nodule defect geometry rapidly returns to the perfect stack geometry. By comparing the EFSW pattern along the axis of symmetry to that along the line at r = 5 μm (that is, to the EFSW pattern of a perfect HR stack), we see that the peak electric field enhancement for this particular geometry is approximately a factor of 2.2. This peak electric field enhancement is determined by comparing the peak electric field in the lossier material (that is, in one of the HfO_2 quarter-wave layers or in the HfO_2 seed) in the nodule defect geometry to the peak electric field in the lossier material (that is, in the first HfO_2 quarter-wave layer) in the perfect HR stack. Note that a peak electric field enhancement of 2.2 corresponds to an enhancement in the heat generation (σE^2) of a factor of 4.8 since the heat generation is proportional to the square of the electric field.

Figure 3 shows the heat generation distribution (in W/μm^3) that corresponds to the electric field profile shown in **Fig. 2**, assuming electrical conductivities of 1.1956 S/m and 0.3366 S/m for HfO_2 and SiO_2, respectively. Since the heat generation is calculated as σE^2, it is evident that the peaks in the electric field profile that lie in the lossier material (the material with the higher electrical conductivity, σ) will be emphasized in the heat generation profile, while the electric field peaks in the less lossy material will be de-emphasized in the heat generation profile. Typically, the electric field enhancements in the lossier material (that is, in the HfO_2 layers) are of the most importance since they will lead to "hot spots" in the heat generation (σE^2) distribution and will therefore control the damage threshold of the HR coating.

Several conclusions can be drawn from the 2-1/2-D EM modeling results for the matrix of 23 different nodular defect geometries. It was found that the dependence of the electric field distribution, the electric field enhancement, and the heat generation on the nodular defect geometry (for example, seed diameter, seed depth, and seed material composition) is, in general, quite complex. Variations in the nodular defect geometry not only

affect the peak value of the electric field in the geometry, but also the electric-field profile itself. As the geometry parameters are varied, the locations of the "hot spots" migrate within the geometry.

It was determined that the highest electric field enhancements occur along the axis of symmetry, with the highest electric field enhancement of 6.4 reported for the largest, most shallow HfO_2 seed (d = 1.5 μm and T = 1 μm), and the lowest electric field enhancement of 1.3 reported for the smallest, most deeply embedded HfO_2 seed (d = 0.25 μm and T = 2.94 μm), corresponding to enhancements in the heat generation by factors of 41 and 1.7, respectively. For small seeds (d ≤ 1 μm), the important factor influencing electric field enhancement is the seed depth, with an increasing seed depth leading to a decreasing electric field enhancement.

On the other hand, for deeply embedded seeds (T ≥ 2.94 μm), the important factor influencing the electric field enhancement is the seed size, with an increasing seed diameter leading to an increasing electric field enhancement. Trends for some of the other nodular defect geometries are not as clear, indicating that perhaps other complex effects such as resonance or other higher-order EM interactions may be the dominant influences on electric-field enhancements for those cases. These results predict that, as a general rule-of-thumb, geometries containing large, shallow seeds lead to the largest electric-field enhancements (or, equivalently, to the highest heat generation) while geometries containing small, deep seeds lead to the smallest electric field enhancements (or, equivalently, to the lowest heat generation).

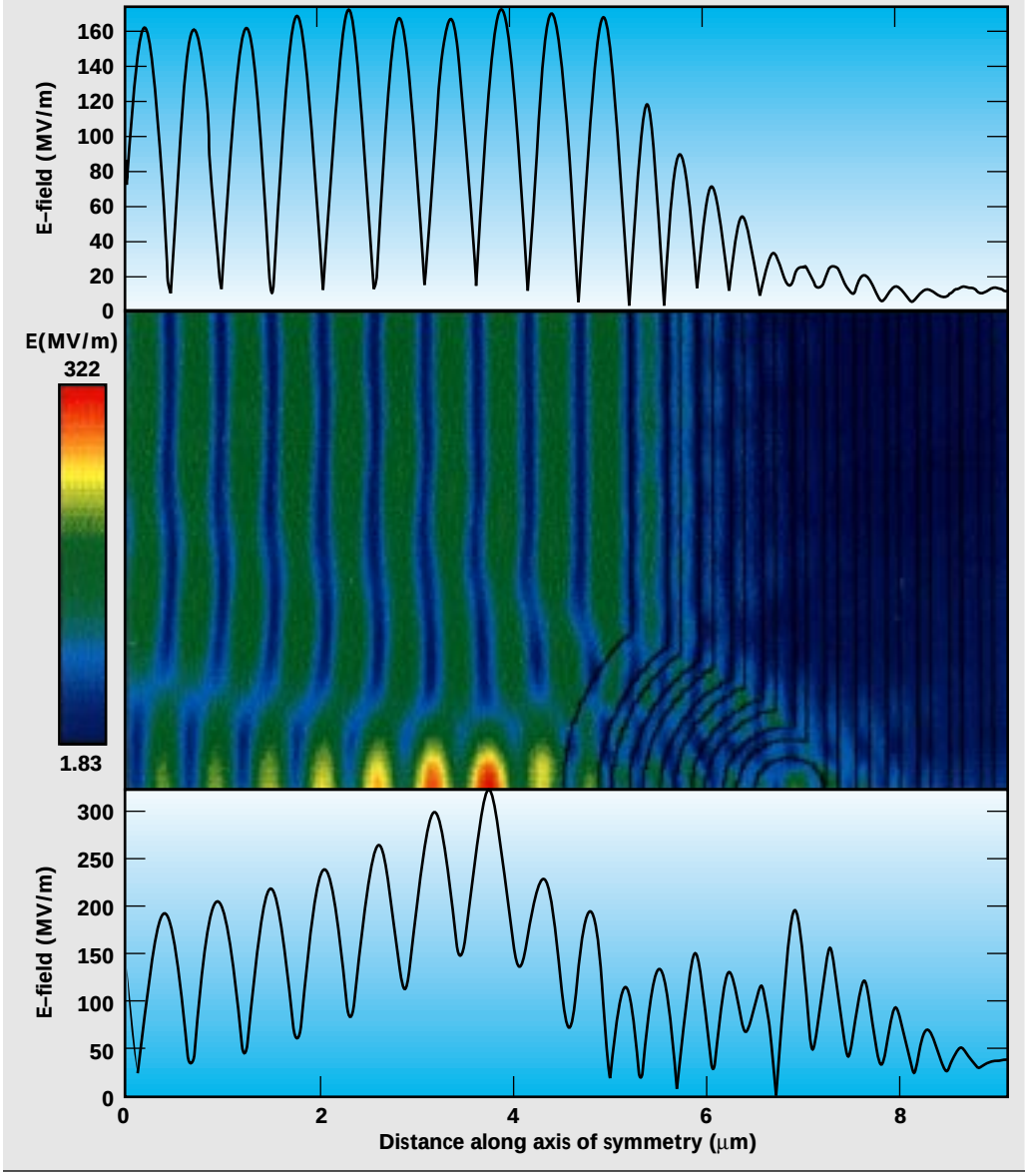

Figure 2. The steady-state electric field profile everywhere within a 2-D r-z cross-section (for ϕ = 0°) of a typical nodular defect geometry, consisting of a spherical HfO_2 seed of diameter, d = 0.73 μm and depth, T = 1.97 μm. Also shown is the EFSW pattern along the axis of symmetry (r = 0 μm) of the nodule as well as the EFSW pattern along a line parallel to the axis of symmetry but at a radius of 5 μm.

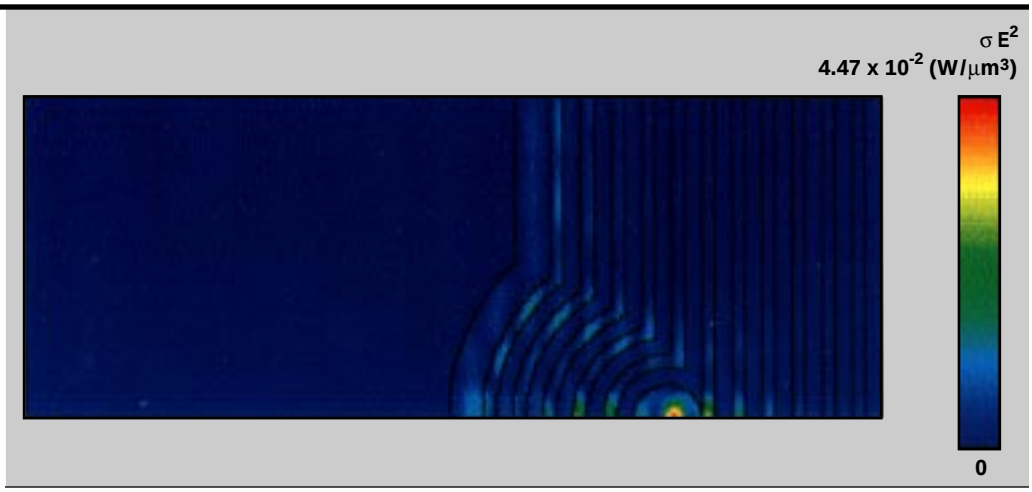

Figure 3. The heat generation distribution (σE^2, in $W/\mu m^3$) that corresponds to the electric field profile shown in Fig. 2, assuming electrical conductivities of 1.1956 S/m and 0.3366 S/m for HfO_2 and SiO_2, respectively.

These conclusions are in close agreement with earlier modeling work reported by DeFord,[7,8] as well as with experimental work reported by Kozlowski.[8] Kozlowski found that nodular defects with large dome heights (particularly those above 0.6 μm) were the most susceptible to laser damage, a result supported by our conclusion that large, shallow defects lead to the highest electric field enhancement and, therefore, the highest heat generation.

Future Work

In the future, the EM modeling of nodular defects in high-power optical coatings could be extended to the fully 3-D regime, allowing for both generalized sources (arbitrary angle-of-incidence and arbitrary polarization) and generalized defect geometries (asymmetric geometries). Once available, the 3-D frequency-domain EM code, EIGER,[9] would be well-suited to perform this 3-D EM analysis.

Coupled engineering codes are being applied to the analysis and design of high-average-power microwave components for Accelerator Production of Tritium (APT).

Acknowledgments

The authors would like to acknowledge T. A. Reitter and A. B. Shapiro for their work in the TOPAZ/NIKE thermal-mechanical modeling effort for the 2-1/2-D nodular defect study, and F. Y. Genin and C. J. Stolz for their experimental investigation and insight into material properties and coating failure mechanisms. We would also like to acknowledge useful discussions with J. F. DeFord of Ansoft. In addition, we wish to acknowledge T. Swatloski, now with TGV, for her contributions in computer science support for this project, and P. P. Weidhaas of LLNL for his contributions in developing the PREAMOS preprocessor. We also acknowledge R. M. Sharpe and J. B. Grant of LLNL for useful discussions about the EIGER code. Finally, our thanks to L. Ahboltin for her excellent administrative support.

References

1. Molau, N. E., H. R. Brand, M. R. Kozlowski, and C. C. Shang (1996), *2-1/2-D Electromagnetic Modeling of Nodular Defects in High-Power Multilayer Optical Coatings*, Lawrence Livermore National Laboratory, Livermore, Calif., (UCRL-ID-124808).

2. Molau, N. E., C. C. Shang, F. Y. Genin, M. R. Kozlowski, H. R. Brand, and R. H. Sawicki (1995), *Electro-mechanical Modeling of Nodular Defects in High-Power Multilayer Optical Coatings*, Lawrence Livermore National Laboratory, Livermore, Calif., (UCRL 53868-95), **1**, p. 7.

3. Shapiro, A. B., D. R. Faux, T. A. Reitter, and R. A. Riddle (1996), "Characterization of Laser-Induced Mechanical Failure Damage of Optical Components," *Engineering Research, Development and Technology FY96 Thrust Area Report*, Lawrence Livermore National Laboratory, Livermore, Calif., (UCRL 53868-96).

4. DeFord, J. F., G. D. Craig, and R. McLeod (1989), "The AMOS (Azimuthal Mode Simulator) Code," *Proceedings of the 1989 Particle Accelerator Conference, Chicago, Ill.*, Mar. 20–23, p. 1181.

5. Shang, C. C., and J. F. DeFord (1990), "Modified-Yee Field Solutions in the AMOS Wakefield Code," *Proc. 1990 Linear Accelerator Conf., Albuquerque, New M.,* September.

6. Mur, G. (1981), *IEEE Trans. Electromagn. Compat.*, **EMC-23**, p. 1073.

7. DeFord, J. F., and M. R. Kozlowski (1993), "Modeling of Electric-Field Enhancement at Nodular Defects in Dielectric Mirror Coatings," *Laser-Induced Damage in Optical Materials: 1992,* (SPIE) Vol. **1848**, pp. 455–473.

8. Kozlowski, M. R., J. F. DeFord, and M. C. Staggs (1993), "Laser-Damage Susceptibility of Nodular Defects in Dielectric Mirror Coatings: AFM Measurements and Electric-Field Modeling," *Proceedings of Second International Conference on Laser Ablation, Knoxville, Tenn.*, April 19–22.

9. Sharpe, R. M., J. B. Grant, W. A. Johnson, R. E. Jorgenson, D. R. Wilton, D. R. Jackson, and J. W. Rockway (1995), *EIGER: A New Generation of Computational Electromagnetics Tools*, Lawrence Livermore National Laboratory, Livermore, Calif., (UCRL 53868-95), **1**, p. 33.

EIGER: Electromagnetic Interactions Generalized

Robert M. Sharpe and J. Brian Grant
Engineering Research Division
Electronics Engineering

William A. Johnson and Roy E. Jorgenson
Sandia National Laboratories
Albuquerque, New Mexico

Donald R. Wilton and Nathan J. Champagne
University of Houston
Houston, Texas

John W. Rockway
Naval Command and Control Ocean Surveillance Center
San Diego, Calif.

New software engineering methods, specifically, object-oriented design, are being used to abstract the key components of spectral analysis methods so that the tools can be easily modified and extended to treat new classes of problems. This software design method also yields a code suite that is more easily maintained than standard designs. This report gives a brief update and highlights planned future developments.

Introduction

The EIGER (Electromagnetic Interactions Generalized) development project is a multi-institutional collaboration that is bringing a variety of spectral domain analysis methods into a single integrated software tool set. Staff from the Sandia National Laboratories, the Navy (NCCOSC/NRaD), Lawrence Livermore National Laboratory, and the University of Houston are collaborating to develop this package which has an unparalleled ability to take general purpose analysis methods and optimize the approach used for specific applications.

The object-oriented design method enables the abstraction of the basic underlying components of computational electromagnetics to yield a suite of tools with unprecedented flexibility. The key components of the numerical analysis and their roles are:

1) elements, which are used to describe the geometry,
2) basis (expansion) functions, which interpolate the unknowns (for example, fields) locally, and
3) operators, which are the underlying formulation of the physics used to propagate the energy or enforce fundamental principles.

By contrast, in standard design procedures entire codes are developed around a single element with a specialized basis function for a specific operator. Although such tools can be used effectively to model large classes of problems, it is often very difficult, if not intractable, to extend the tools beyond their initial design. Overcoming this limitation is one of the most compelling goals of our project. Indeed, the applicability of EIGER is significantly broadened as we cast a variety of analytic treatments (Green's functions) into a form compatible with the numerical procedures in EIGER.

The following sections briefly describe this year's efforts in several key areas.

Progress

Elements

Elements are the basic building blocks that are used to describe a given geometry for numerical computation. Elements are typically the output of a commercial mesh generation package that has discretized a solid CAD model into pieces that are

amenable to numerical computation. A pre-processor then reads these elements and assigns such features as material characteristics and excitation parameters to generate the actual input for the physics code.

Our development team has been using two commercial CAD and mesh generation packages to generate the element descriptions for a given problem. Specifically, MacNeal Schwendler's CAD tool PATRAN and SDRC's IDEAS are being used to feed the electromagnetics analysis tools. Even though these packages were primarily designed to generate computational meshes and information for mechanical engineering analysis, they have proven flexible enough to label and group information associated with a mesh such that EIGER can easily take advantage. IDEAS advanced grouping functionality has proven especially useful for generating compute meshes for complicated geometries.

The EIGER suite can treat both 2- and 3-D problems in a single integrated tool set. Initially, emphasis was placed on the requirements for modeling surface physics. Thus, for 2-D geometries, combinations of linear segments or "bar" elements are currently used to describe the surface problem. Likewise, for 3-D geometries, both linear triangles and rectangles can be combined to render accurate surface models. In addition to the basic elements for modeling 3-D surfaces, wire segments are also incorporated into EIGER. Currently, at the University of Houston a scheme is being implemented to use higher-order surface elements to more accurately resolve the geometry of curved objects.

The code structures have been designed to easily incorporate volumetric elements directly into the analysis framework. In fact, the 3-D surface elements are all that are required for 2-D volumetric analysis. Currently, general 3-D volumetric elements such as tetrahera, hexahedra, and pentahedra are being added to the code suite to address general finite element problems.

Basis Functions

Basis (or expansion) functions are used to locally interpolate an unknown quantity in many numerical methods. These unknowns may physically represent surface currents or fields for dynamic operators, or potentials for statics. Both constant and linear basis functions are currently available for each of the elements described above. The characteristic integrals (for integral equation solutions) that arise in many problems require that the potentials, and their gradients due to source distributions that are represented by these basis functions, must be efficiently computed.

Extensive efforts have enabled most of these calculations to be cast into the same basic form, thus simplifying their integration into a general purpose code. In conjunction with the efforts to add higher-order elements, extensions are currently under investigation to use higher-order (smoother) basis functions to enable a more efficient numerical solution for electrically large problems. In addition, we have developed a new formulation for singular basis functions that will incorporate known edge conditions and other known local variations directly into the numerical procedure.

Operators

An electromagnetic operator is a mathematical construct that relates the field at a point to the sources that produced the field. Since previous efforts focused initially on incorporating surface physics, emphasis was placed on integral operators, which are among the most efficient classes of operators for enforcing this type of physics. These operators explicitly propagate a field between locations. The numerical solution of these operators is known as the method of moments. Specific integral operators are often given specific names that are related to boundary conditions that are applied and the manner in which they are enforced. A variety of integral operators have been incorporated into EIGER to treat the following boundary conditions: perfect electric conductors, conductors coated with complex impedance materials, and homogeneous dielectrics (penetrable materials). Specifically, these operators are:

1) the Electric Field Integral Equation (EFIE);
2) the Magnetic Field Integral Equation (MFIE);
3) the Combined Field Integral Equation (CFIE); and
4) general Homogeneous Lossy Dielectrics (PMCHW).

The basic formulation for the integral operators has been generalized and simplified so that all of the above operators are generated by simply taking linear combinations of basic coupling or interaction operators. This powerful abstraction means that a variety of other boundary conditions can easily be added to the code simply by choosing the appropriate set of coefficients (that is, equivalent aperture formulations, and alternative dielectric treatments).

This year, efforts were begun to add the types of finite-element operators that are required to solve partial differential equations. Rigorous treatments for 2-D finite element solutions of both electrostatic and magnetostatic problems were incorporated for the analysis of micro-electro-mechanical devices (MEMs). Specific numerical treatments were

designed to allow the termination of the finite element volumetric mesh with the appropriate surface mesh using an integral operator. Currently, efforts are underway to extend these same capabilities to the fully 3-D case.

Green's Functions

A Green's function can be thought of as a characteristic solution of a problem for an ideal infinitesimal source. Ideally, this solution directly satisfies as many of the boundary conditions as possible in an analytic fashion, thus reducing the numerical requirement for a given problem. One of the most promising features of the EIGER development is the ability to directly incorporate a variety of Green's functions into the solution. In addition to the standard homogeneous free-space type Green's functions, this year a completely unique capability was added to EIGER by using a multi-layered media Green's function that can treat arbitrarily-shaped objects that are penetrable. These extensions allow applications to be addressed in a variety of areas such as multi-layered electronic circuit boards, high-powered optical mirrors, and geophysical problems.

In **Fig. 1** the scattering from a dielectric cube ($\varepsilon_r = 2.9$) immersed in a half space with a dielectric constant of 3.0 is shown. The results are compared with a Born approximation and the agreement is seen to be quite good.

Solvers and Post-Processing

An end user of EIGER has a choice of basic numerical solutions of linear systems by either a Gaussian elimination method or a bi-conjugate gradient method. The later method is extremely useful for large systems of equations. Solvers that are tuned for the sparse systems that arise from a finite element solution are also planned for incorporation into the code.

Post-processing capabilities currently include the calculation of near or far fields from the basic current solutions. **Figure 2** shows the geometry of a commercial broadband horn made by AEL which is designed to operate between the frequencies of 1 and 10 GHz. Multiple compute meshes were generated for the geometry, ranging from 2000 to about 8000 unknowns.

Figure 3 shows the 3-D radiation pattern for the antenna at a frequency of 5 GHz. This pattern consists of roughly 16,000 field points.

Figure 4 shows the radiation pattern at a frequency of 10 GHz. The maximum directivity is used to calculate a directive gain for the antenna. **Figure 5** depicts the calculated gain vs frequency as compared to measured data for the structure.

Future Work

Each of the areas outlined above will continue to evolve and extend to reach broader classes of problems with a greater diversity of tools. Specific examples of future development are briefly noted here.

As mentioned previously, we are extending the element modules of the code to include higher order elements. These elements can be of arbitrary order, and will more accurately resolve the local

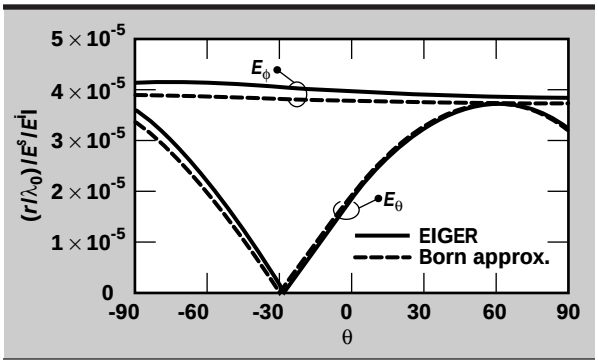

Figure 1. The scattered far field in the $\phi = 0°$ plane from a small dielectric cube ($\varepsilon_b = 3.0\varepsilon_0$). The plane waves are incident from $\theta^i = 60°$ and $\phi^i = 0°$.

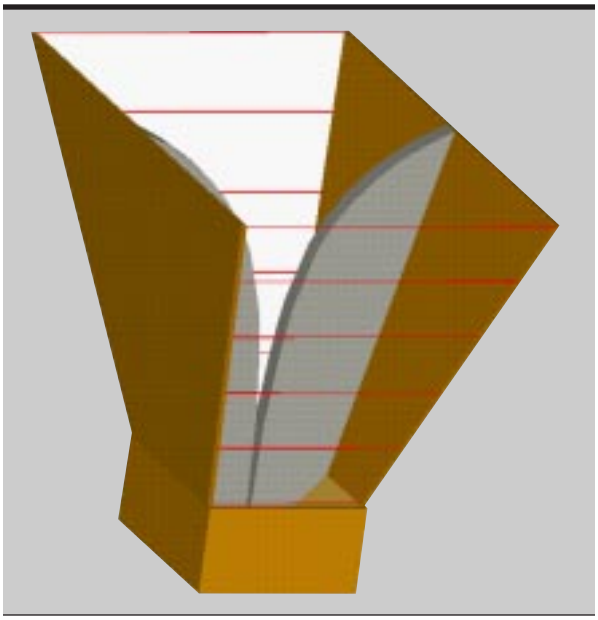

Figure 2. CAD representation of a commercial flared notch horn antenna made by AEL.

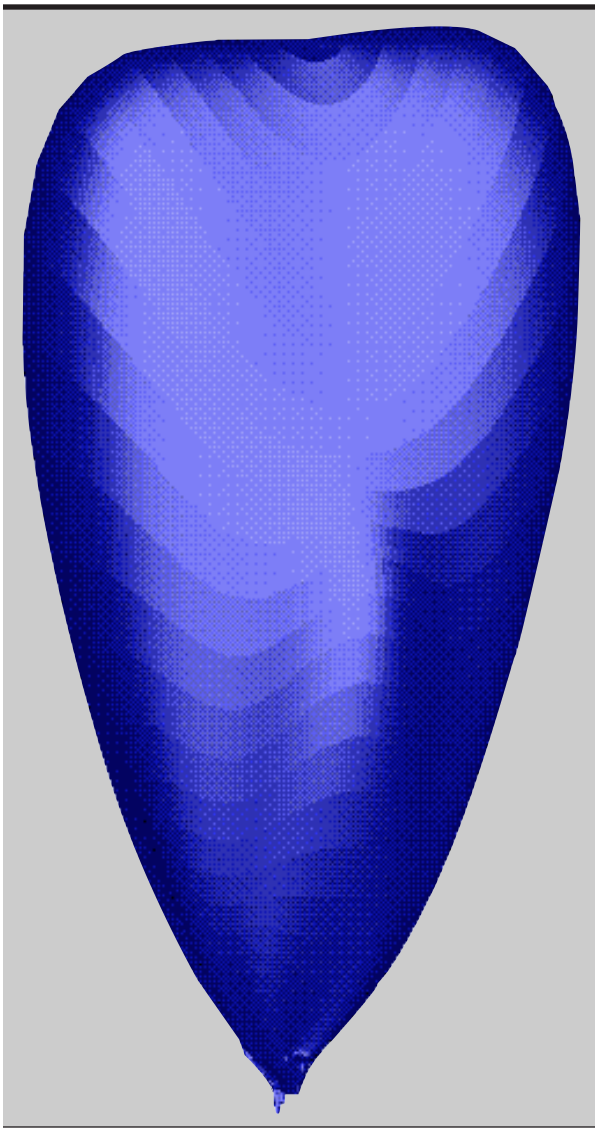

Figure 3. Three-dimensional radiation pattern for the AEL horn at 5 GHz.

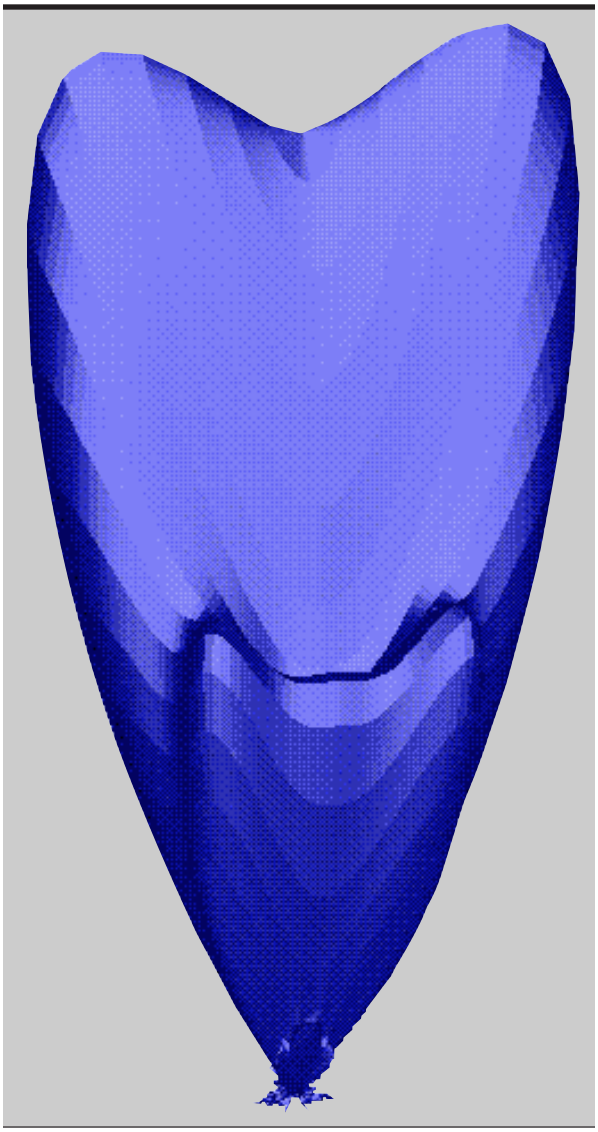

Figure 4. Three-dimensional radiation pattern for the AEL horn at 10 GHz.

Figure 5. Antenna gain (directivity at bore sight) vs frequency. Both measurements and experiments are shown.

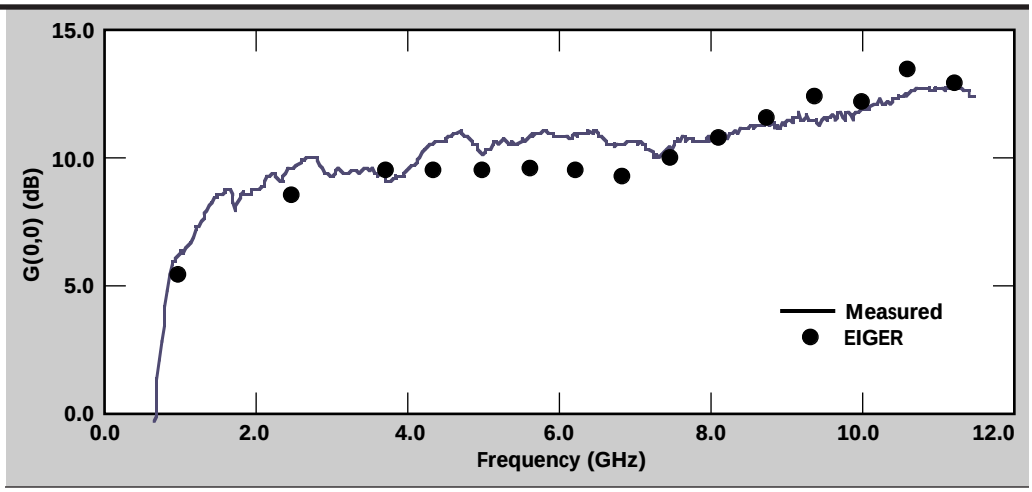

variations of the geometry. Also, volume elements will be incorporated for treating inhomogeneous material regions.

The combined versatility of elements and basis functions suggests multiple combinations and approaches to solve models, possibly overwhelming the modeler with choices. However, this versatility also provides the flexibility to tackle portions of the model with the most appropriate combinations. During this past year, key steps were taken to address the increased complexity of effectively using a code suite such as this. Efforts will continue to develop and extend the pre-processor interface to the physics tools for more efficiency. This activity is being performed in conjunction with the TIGER effort, also described in this publication.

Additional integral operators will continue to be added to the EIGER suite. In addition, the differential operators, which are the underlying mathematics, are being extended from 2-D to 3-D.

Extensions to the Green's functions in the code are also underway. General symmetry treatments have been added to the analysis code and are being incorporated into the post-processor. In addition, an effort to incorporate general periodic analysis, that was previously developed for treatment of cavities and array analysis is also underway.

Another key area for the coming year is the efficient migration of this tool set to advanced computer architectures. Both symmetric multiprocessor (SMP) and massively-parallel processor (MPP) systems are targeted, and work is being done on both the physics kernel and the associated numerical linear algebra routines.

Acknowledgment

The authors wish to thank T. Rosenbury for providing the measured results for the directive gain on the AEL horn antenna used in **Fig. 5**.

Laser Drilling Modeling

David J. Mayhall and Jick H. Yee
Engineering Research Division
Electronics Engineering

We have modified an existing, one-dimensional, laser drilling computer code to run on an IBM-compatible PC, investigated some of the code's behavior, estimated the pressure pulse transmitted to two different solid materials due to laser ablation, and modestly enhanced the code's user interface.

Introduction

Laser drilling and laser shock generation are being explored to an increasingly greater extent for various manufacturing processes, such as circuit-board machining, metal surface hardening, and parts forming in powder metallurgy. In these endeavors, potential increases in efficiency and reductions in expense result from understanding the complex physical and chemical processes between the laser light and the materials upon which it impinges and ablates. Sufficiently accurate computational modeling of the laser ablation of materials should yield improved understanding of the processes involved.

As a step in the computer modeling of laser ablation for manufacturing, we have embarked on a laser drilling modeling project. The objectives of this project are 1) to convert a one-dimensional, laser drilling computer code, DRILL[1], which was written in Hewlett-Packard (HP) FORTRAN on an HP workstation with a UNIX operating system, to run on an IBM-compatible, Pentium-class PC; 2) to benchmark PC run results against HP workstation results; 3) to improve the code's user-related graphics capabilities; and 4) to improve the physics models in the code.

Progress

We transferred a version of the DRILL computer code to a Gateway 2000, model P166, 166 MHz Pentium PC and modified it to run under the Windows 95 operating system with Microsoft Power Station FORTRAN 90. After running a problem for atmospheric air over solid aluminum with supplied input and data files to completion at 5 μs, we benchmarked the calculated results against the results for the same input and data files from an HP series 700 workstation. The agreement between the results was excellent.

We then performed a set of computer runs by varying the peak laser incident pulse intensity and the pulse length. With the initial 120-ns-long laser pulse and spherical vapor expansion into the air, the code ran to completion for peak laser intensities of 3×10^8 and 1×10^9 W/cm^2. At 5×10^9 W/cm^2 of peak incident laser intensity, the code suffered a

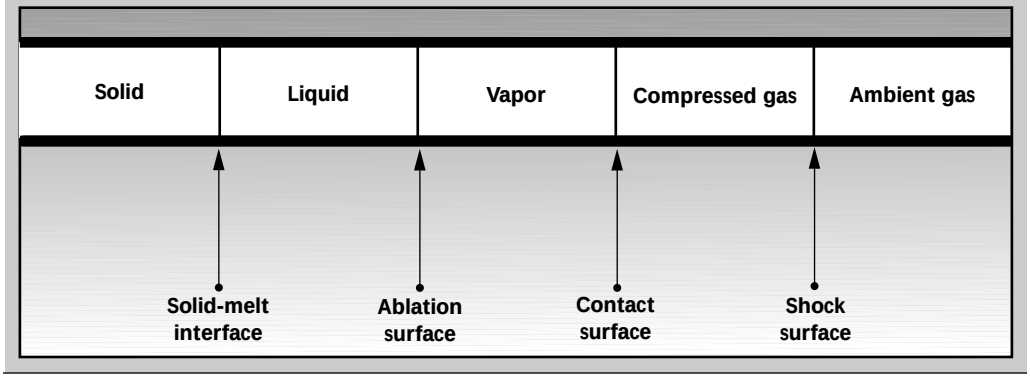

Figure 1. Schematic arrangement of the evolved material regions.

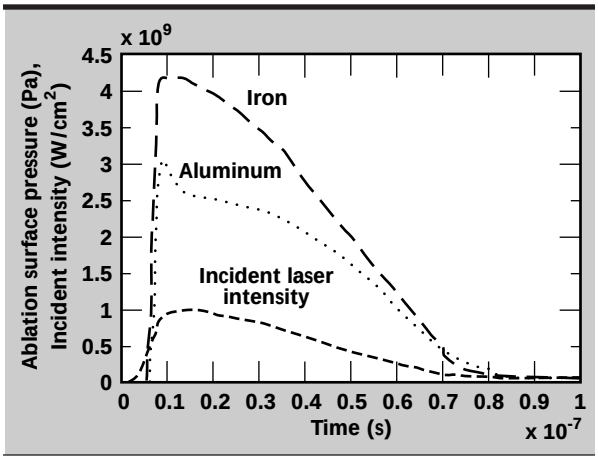

Figure 2. Calculated ablation surface pressure vs time for aluminum and iron solids at peak incident laser intensity of 1×10^9 W/cm^2.

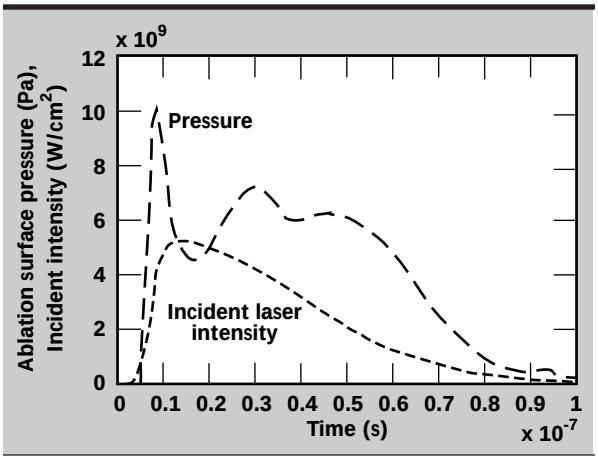

Figure 3. Ablation surface pressure for iron at 5×10^9 W/cm^2.

dramatic slowdown in integrator time step. It ran for several hours, but could not proceed past about 18.6 ns in simulation time. At 5×10^9 W/cm^2, with the original laser pulse truncated to 20 ns, the code ran to completion. At 1×10^{10} W/cm^2, with the truncated incident pulse, the integrator in the code was unable to achieve corrector convergence beyond 6.98 ns into the simulation. The reason for the inability to obtain solutions at the higher incident laser intensities is not yet known.

Several runs with atmospheric air over iron were investigated next, with spherical vapor expansion into the air. The code ran to completion with the initial incident laser pulse at 1×10^9 and 5×10^9 W/cm^2 of peak intensity, but encountered the time-step slowing down problem at about 26.0 ns into the simulation, with a peak incident intensity of 1×10^{10} W/cm^2.

When a sufficiently intense laser pulse impinges on most solid materials, it melts the surface of the material. If the incident pulse continues, the melted, liquid layer expands into the solid. As this occurs, the liquid surface vaporizes, and a vapor front expands into the ambient gas over the solid. The ambient gas is then compressed, and a shock surface is generated. This array of material phases is schematically portrayed in **Fig. 1**, which has been adapted from Reference 1. The time-varying thicknesses of the regions beyond the solid are usually on the order of microns.

The pressure/time history at the ablation surface is one calculated quantity of interest to the developers of some manufacturing processes. This pressure/time history is an estimate of the pressure pulse transmitted into the solid. **Figure 2** shows the calculated ablation surface pressure/time history for aluminum and iron solids at a peak incident laser intensity of 1×10^9 W/cm^2. The time history of the incident laser pulse is also shown. **Figure 3** shows the ablation surface pressure for iron at 5×10^9 W/cm^2 of peak incident intensity. These peak pressures agree roughly in order of magnitude with those reported in the literature on experimental investigations for metal ablation.

We next added comment lines to the input file and the source output routine to describe briefly the input parameters and output arrays for a code user. These modifications allow a user to more easily know what physical quantities the input parameter and output array names represent.

References

1. Boley, C. D., and J. T. Early (1994), "Computational Model of Drilling with High Radiance Pulsed Lasers," *Proc. ICALEO '94, Orlando, Fla.*, pp. 499–508.

Technical Information Department
Lawrence Livermore National Laboratory
University of California
Livermore, California 94551